


Article

Experimental and Numerical Study of Suspended Inter-Array Cable Configurations for Floating Offshore Wind Farm

Di-Rong Li, Yu-Shiou Su and Ray-Yeng Yang * 

Department of Hydraulic and Ocean Engineering, National Cheng Kung University, Tainan City 70101, Taiwan
* Correspondence: ryyang@mail.ncku.edu.tw

Abstract: The present study evaluates the feasibility of using a fully suspended inter-array cable system for an offshore wind farm. It includes both numerical simulations and a scaled-down experiment, conducted at a 1:49 scale, to validate the numerical results. To achieve the goal, a 15 MW floating offshore wind turbine (FOWT) and a floating offshore substation (FOSS) are involved to simulate the wind farm array. This study incorporates the 50-year return period conditions of the Taiwan Hsinchu offshore area, which has a water depth of about 100 m, to validate the specifications related to the platform motion and mooring line tension. Additionally, an analysis of the tension, curvature, and fatigue damage of the dynamic cable system is discussed in this research. Because a fully suspended cable is a relatively new concept and may be more frequently considered in a deeper water depth area, numerical simulation software Orcina Orcaflex 11.4 has been chosen to conduct the fully coupled simulation, determining whether the fully suspended cable system could effectively withstand the challenges posed by extreme sea conditions. This is due to the reason that a fully suspended cable would occupy a larger space in the ocean, which may pose a risk by influencing the navigation of the vessels. Therefore, the cable laying depth under normal sea states is also discussed to evaluate the influence over vessel navigation. This study also collects the long-term environmental data from the Central Weather Bureau, Taiwan, to calculate the accumulative cable fatigue damage under different sea states. To integrate the results, this research applies fitness parameters to evaluate the feasibility of each cable configuration. Covering the cable performance under extreme sea states and regular operating sea states offers valuable insights for applications in ocean engineering.

Keywords: floating offshore wind turbine; floating substation; suspended cable; numerical simulation; large flume experiment



Citation: Li, D.-R.; Su, Y.-S.; Yang, R.-Y. Experimental and Numerical Study of Suspended Inter-Array Cable Configurations for Floating Offshore Wind Farm. *J. Mar. Sci. Eng.* **2024**, *12*, 853. <https://doi.org/10.3390/jmse12060853>

Academic Editors: Constantine Michailides, Wei Shi and Jianhua Zhang

Received: 26 March 2024
Revised: 8 May 2024
Accepted: 14 May 2024
Published: 21 May 2024



Copyright: © 2024 by the authors. Licensee MDPI, Basel, Switzerland. This article is an open access article distributed under the terms and conditions of the Creative Commons Attribution (CC BY) license (<https://creativecommons.org/licenses/by/4.0/>).

1. Introduction

In response to the net-zero carbon emission policy in Taiwan, the government is actively developing green energy. With the development of offshore wind farms and the launch of large-scale wind turbines, the power generation of wind farms is also gradually expanding. However, electricity is prone to loss due to long-distance transmission at low voltage, resulting in poor power generation efficiency, and even under the layout of too many cables, the coastal environment is also damaged. Therefore, offshore substations can collect the power generated by the wind turbines in the wind farms, and after boosting the voltage, it will be transported to onshore facilities by export cables, which can solve this problem. In addition, the form of offshore substations is no longer limited to fixed foundations. The Fukushima FORWARD (Fukushima Floating Offshore Wind Farm Demonstrator) project, for example, utilizes floating platforms as its foundation (Yoshimoto et al., 2013) [1]. In addition to its substation function, the Fukushima floating offshore substation is equipped with observation towers and helipads, providing facilities for investigating nearby sea wind conditions. Ideol and Atlantique Offshore Energy (AOE) jointly developed a floating offshore substation using a barge-type floating platform. The barge-type floating offshore substation, designed with patented damping pool technology,

can operate in the world's most extreme environments and offers modular manufacturing capabilities (Ideol, 2019) [2]. In the United States, numerical validations were conducted for local wind field sea conditions, analyzing the motion attitudes of the semi-submersible platform carrying the substation and the tension of the mooring cables under extreme weather conditions. The results indicate that the stability of this platform meets regulatory limits and can support floating wind farms in deeper waters, such as those off the northeastern United States and other regions (Shelley et al., 2020) [3]. Therefore, it can be expected that the future development of offshore substations will continue to move toward deep-sea construction in a floating form. However, the current designs of dynamic cable systems are based on experiences from risers used for oil transmissions, such as lazy wave and lazy S configurations (CIGRE Working Group B1.40, 2015) [4]. These types require burying the cables on the seabed. This approach occupies seabed space and raises concerns about the potential ecological disruption during the construction process. Therefore, it is necessary to study fully suspended dynamic cables that can keep the cables safe during typhoons and seek different dynamic cable configurations that can reduce costs and environmental damage.

A comparison of dynamic and static cables was proposed by Ikhennicheu et al. (2020) [5]. To meet the increasing demands on dynamic cables, including the need to withstand higher loads from waves and currents, the material composition of these cables must exhibit greater rigidity, resistance to bending, and torsional resilience. Additionally, it is crucial to ensure improved fatigue resistance, especially when these cables are exposed to prolonged wave conditions. Compared to the manufacturing process of static cables, the fabrication of dynamic cables is more intricate and time-consuming due to these specialized requirements. To gain a deeper understanding of the mechanics governing dynamic cable systems in offshore structures, Thies et al. (2012) [6] conducted a comprehensive study focusing on cable tension, curvature, and fatigue damage. In their research, they segmented the characteristics of a three-core dynamic cable into cable segments and buoy segments. Within these segments, they defined several critical parameters, including the outer radius, bending stiffness, axial stiffness, minimum breaking load, and minimum bending radius. Moreover, they established values for the nominal weight of both cable and buoy segments in air and seawater conditions.

These meticulously defined parameters have indeed played a pivotal role in informing and shaping subsequent studies related to dynamic cables. They have contributed to ensuring a more accurate and comprehensive understanding of the behavior and performance of dynamic cables in offshore applications. In addition to the focus on the mechanical behavior of dynamic cables, Sobhania et al. (2020) [7] introduced a fatigue calculation process specifically tailored to dynamic cables. This innovative approach involves the consideration of various sea state conditions for simulation. To determine the fatigue damage incurred under different environmental conditions, the rain flow method is employed. This method provides a systematic way to analyze and calculate the fatigue damage, considering the cyclic loading patterns experienced by the dynamic cables over time.

By incorporating this fatigue calculation process, researchers and engineers can better assess the long-term durability and reliability of dynamic cables in offshore environments, enhancing the safety and performance of these critical components in renewable energy infrastructure. Srinil (2016) [8] introduced a novel W-shaped fully suspended configuration for dynamic cables, suggesting that this configuration is suitable for inter-array cable deployment in offshore wind farms. This design incorporates buoyancy blocks to reduce the tension in the dynamic cables and make them more responsive to environmental forces. The key aspect of this configuration is the precise design of the buoyancy segments, which must provide adequate buoyancy to the cable. This ensures that the cable remains unaffected by the wave forces, thereby preventing significant deformation. Shi et al. (2022) [9] also mentioned that the W-shaped configuration is less susceptible to water depth limitations and can effectively reduce construction costs. However, the maturity of their technology is still in its early stages. Moreover, there is currently limited research on this

type of suspended cable configuration, especially concerning the experimental aspects. Schnepf et al. (2023) [10] analyzed the different configurations of suspended dynamic cable tension between the FOWT and FPSO in deep water. Beier et al. (2023) [11] presented dynamic cable fatigue results for two spar-type FOWTs. They also explained that fatigue values tend to accumulate more at the platform connection points. All the relevant studies are confined to numerical simulation research, and there remains a scarcity of results from experimental models. Ahmad et al. (2023) [12] presented a method for optimizing the design of the power cable configuration between two FOWTs. It takes into consideration the environmental conditions of the Norwegian Sea and assesses the impact of marine growth on the cables. The analysis focuses on the cable effective tension, minimum bending radius, and horizontal offset of the cables.

This study adopts a suspended dynamic cable design, taking inspiration from the W-shaped cable configuration. This research approach begins with conducting scaled experiments and subsequently comparing the results with numerical simulations by Ansys AQWA (2021 R1) and Orcina OrcaFlex to establish the credibility and accuracy of the numerical calculations. Once the validation process is completed, this study proceeds to subject the suspended dynamic cable design to extreme environmental conditions in numerical simulations, particularly in the context of the 100 m water depth in the Hsinchu offshore water area. Within these simulations, this study focuses on analyzing the tension and curvature experienced by the dynamic cable under various conditions. Specifically, it explores the behavior of the cable in response to normal sea conditions and investigates whether the submerged depth of the cable has any implications for vessel navigation in the area. Additionally, the research encompasses a fatigue analysis of the cable, aiming to assess its long-term durability and reliability. To support the fatigue analysis, this study collects data from buoys positioned in the Hsinchu offshore water area. These data are essential for compiling the probabilities associated with different sea state conditions, which in turn inform the calculations related to fatigue accumulation. For the fully suspended cable, it is still a relatively new concept and may be more frequently considered in a deeper water depth area. However, this study employs fitness parameters as a crucial tool for evaluating the suitability and effectiveness of different configurations of the suspended dynamic cable in the target field. By integrating these various analyses and assessments, this research offers a comprehensive understanding of the cable behavior and performance for an FOWT and FOSS, particularly under extreme conditions, contributing valuable insights to the field of offshore renewable energy.

2. Numerical Methods

For the numerical simulations conducted in this study, the commercial software ANSYS AQWA (ANSYS Inc., Southpointe, PA, USA, 2021 R1) [13] was employed to compute hydrodynamic parameters in the frequency domain. These output parameters were subsequently utilized as input data for OrcaFlex (Orcina Ltd., Cumbria, UK, 2022) [14] to perform time-domain simulations.

This study formulated the governing equations for the FOWT and FOSS based on Newton's second law. These equations took the external forces acting on the system into account, which included the wave-induced load acting on the platform and the mooring forces that anchor the system in place. The calculation of wave forces was a critical component of this analysis and was conducted using potential flow theory. This involved the consideration of both wave radiation forces and wave excitation forces. Importantly, because this study focused on extreme wave conditions in shallow water, it appropriately accounted for the second-order wave force component, which is particularly significant in such scenarios. The resulting governing equation, which describes the dynamic behavior of the FOWT and FOSS under these complex forces and wave conditions, was derived through this rigorous methodology. This equation serves as the foundation for further analysis and

simulation, facilitating a comprehensive understanding of the system’s response to extreme environmental conditions.

$$\{m + A\}\ddot{\zeta}(t) = F^{1st}(t) + F^{2nd}(t) + F_M(t) - C\dot{\zeta}(t) - B|\dot{\zeta}(t)|\dot{\zeta}(t) - K\zeta(t) \tag{1}$$

where m is the mass of the floating platform; $F^{1st}(t)$ is the first-order wave excitation force; $F^{2nd}(t)$ is the second-order wave excitation force, called the wave drift force in this study; $F_M(t)$ is the mooring force; C is the linear damping matrix, including the drift damping effects; B is the quadratic damping matrix; K is the total stiffness matrix; A is the added mass matrix at infinite frequency; and $\zeta(t)$, $\dot{\zeta}(t)$, and $\ddot{\zeta}(t)$ represent the displacement, velocity, and acceleration time-series vectors in the translational or rotational motions, respectively.

The second-order wave excitation force is computed using the Quadratic Transfer Function (QTF) data, considering the interactions between all pairs of wave components in the sea state. This sea state is typically a superposition of a specified number, ‘ n ’, of regular wave components present in all the specified wave trains. The wave drift load can be expressed as follows:

$$F_i^{wave(2)}(t) = \int_{-\infty}^{\infty} \int_{-\infty}^{\infty} g_i(\tau_1, \tau_2) \zeta(t - \tau_1) \zeta(t - \tau_2) d\tau_1 d\tau_2 \tag{2}$$

where $g_i(\tau_1, \tau_2)$ is the quadratic impulse response function, τ_1 and τ_2 are the time, and $\zeta(t)$ is the duration of the wave. The details of this wave drift load calculation, which considers the interactions and superposition of the wave components, are essential for accurately modeling the second-order effects in the dynamic behavior of the system.

The obtained frequency-domain hydrodynamic parameters are the inputs to OrcaFlex for numerical simulations in the time domain. OrcaFlex is widely used for stability assessments of offshore floating structures and the design of mooring systems, including ships and FOWTs. The equation for calculating the time domain of the FOWT and FOSS in OrcaFlex is as follows.

$$M(a) + C(v) + K(p) = F(p, v, t) \tag{3}$$

where $M(a)$ = the inertial force of the FOWT and FOSS;

$C(v)$ = the damping force of the FOWT and FOSS;

$K(p)$ = the stiffness force of the FOWT and FOSS;

$F(p, v, t)$ = the external force;

p, v, a, t = the position, velocity vector, acceleration vector, and simulation time, respectively.

Morison’s equation is utilized in OrcaFlex to compute the hydrodynamic forces acting on mooring lines and power cables. This equation is applied to determine the wave loads, encompassing both the inertial forces associated with the fluid acceleration and the drag forces associated with the fluid velocity acting on the bodies.

$$f = (C_m \Delta a_f - C_a \Delta a_b) + \frac{1}{2} \rho C_d A |v_r| v_r \tag{4}$$

where f = the wave load on the structure;

C_m = the inertia coefficient of the structure;

Δ = the drainage volume of the structure;

a_f = the acceleration of the fluid relative to the earth;

C_a = the added mass coefficient of the structure;

a_b = the acceleration of the structure relative to the earth;

ρ = the fluid density;

C_d = the drag coefficient of the structure;

A = the area of the structure subject to fluid resistance;

v_r = the velocity of the fluid relative to the structure.

Additionally, the dynamics of the mooring lines and power cables are simulated based on the lumped mass method. The entire mooring line and power cable are divided into

finite elements and nodes. External forces acting on mooring lines or power cable elements are uniformly distributed to each adjacent node, forming the equations of line motion.

2.1. Model Set Up

In this study, a 1/49 scale model of the FOWT, the FOSS, the mooring system, and the dynamic cable system were used in the hydraulic model test.

2.1.1. Wind Turbine

The wind turbine prototype was based on an IEA 15 MW wind turbine (Gaertner et al., 2020) [15]. To simplify the experiment, this research only considered the wind thrust on the blades. A general drone (Figure 1) was modified to simulate the scaled-down wind thrust based on the Froude similarity.

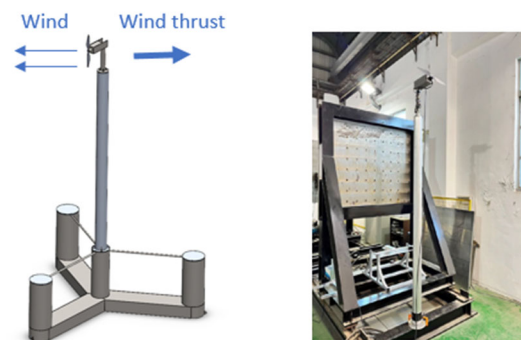


Figure 1. Schematic of the wind turbine.

2.1.2. Floating Platform

Figure 2 shows the floating platform of the wind turbine, for which the design is inspired by the University of Maine (Allen et al., 2020) [16]. According to the substation parameters from Lai (2018) [17], a substation structure with a capacity of 100 MW to 150 MW is 30 m in length, 30 m in width, 20 m in height, and the weight is approximately 1000 tons of prototype. The model is constructed with a scale ratio of 1/49. Figure 3 shows the floating platform of the substation, for which the design is inspired by DeepCWind (Robertson et al., 2014) [18] with slight modifications in the dimensions and consider the air gap proposed in DNVGL-ST-0145 [19]. The detailed prototype dimensions of the floating platforms are as shown in Figures 4 and 5, relevant properties are listed in Tables 1 and 2.

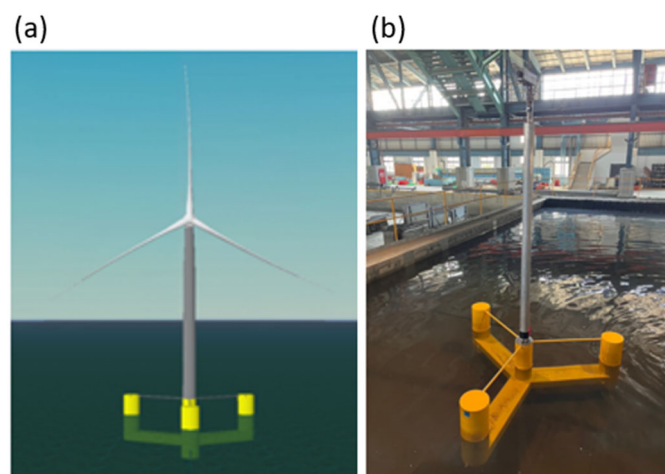


Figure 2. Schematic of VoltturnUS-S floating platform equipped with a 15 MW wind turbine. (a) Full scale and (b) model scale.

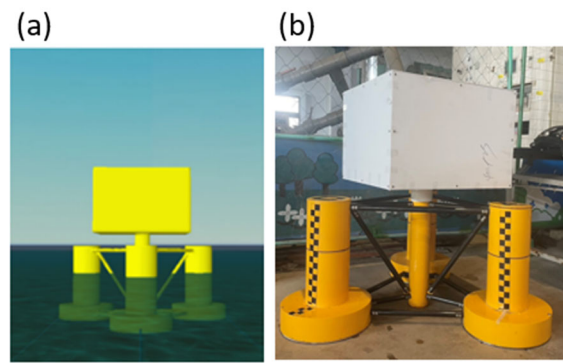


Figure 3. Schematic of DeepCWind floating platform equipped with 100 MW substation. (a) Full scale and (b) model scale.

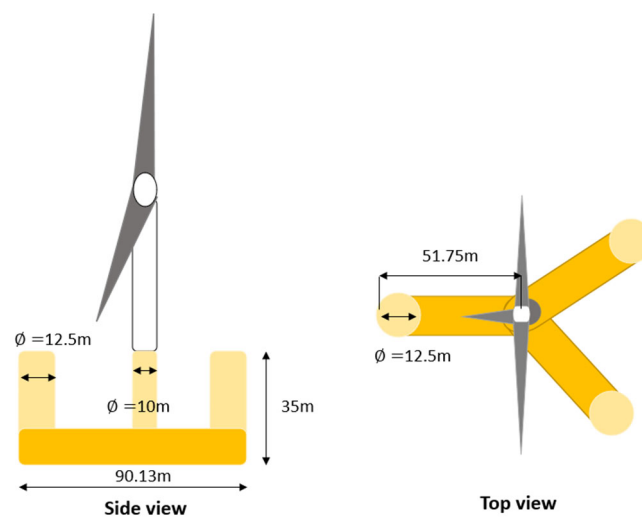


Figure 4. The dimensions of the FOWT.

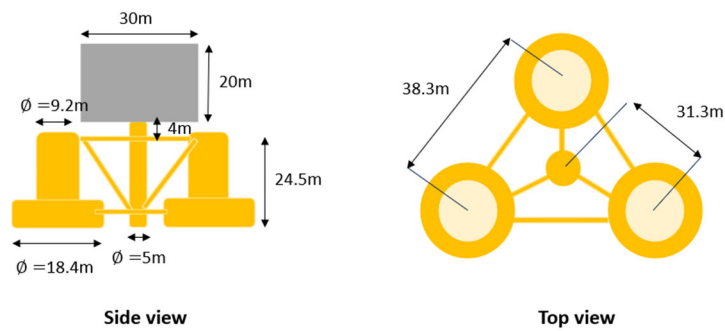


Figure 5. The dimensions of the FOSS.

Table 1. Parameters of the VoltturnUS-S floating platform equipped with a 15 MW wind turbine.

Properties	Full Scale	Model Scale
Total mass	20,131,300 kg	151.8 kg
Draught	20 m	40.8 cm
XCG	0 m	0 cm
YCG	0 m	0 cm
ZCG from sea water level	-2.234 m	-10.3 cm
Roll inertia	4.46×10^{10} kg·m ²	1.58×10^6 kg·cm ²
Pitch inertia	4.45×10^{10} kg·m ²	1.58×10^6 kg·cm ²
Yaw inertia	2.39×10^{10} kg·m ²	8.48×10^5 kg·cm ²

Table 2. Parameters of the DeepCWind floating platform equipped with 100 MW substation.

Properties	Full Scale	Model Scale
Total mass	6,046,619 kg	51.4 kg
Draught	15.31 m	8.16 cm
XCG	0 m	0 cm
YCG	0 m	0 cm
ZCG from sea water level	−4.77 m	−9.73 cm
Roll inertia	$2.66 \times 10^9 \text{ kg}\cdot\text{m}^2$	$9.4 \times 10^4 \text{ kg}\cdot\text{cm}^2$
Pitch inertia	$2.66 \times 10^9 \text{ kg}\cdot\text{m}^2$	$9.4 \times 10^4 \text{ kg}\cdot\text{cm}^2$
Yaw inertia	$3.38 \times 10^9 \text{ kg}\cdot\text{m}^2$	$1.2 \times 10^5 \text{ kg}\cdot\text{cm}^2$

2.1.3. Mooring System

As for the mooring system, this study ensures that the scaled-down mooring lines have the same diameter and unit weight as the prototype. This is done to maintain the same level of restoring force in the mooring lines as in the prototype, thereby reducing any discrepancies caused by the scaling down of the mooring lines. A test of forced displacement was conducted to validate the scaled-down mooring tension; the results in Figure 6 show a good agreement with the numerical simulation.

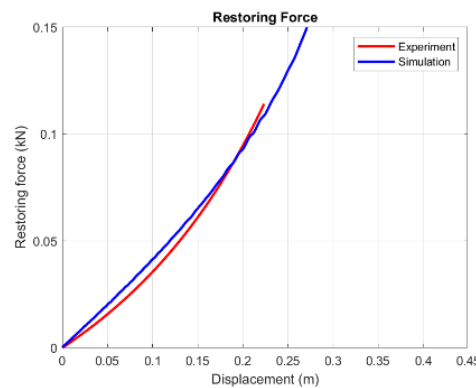


Figure 6. Comparison of mooring restoring force between experiment and numerical simulation.

Due to the limitations of the width of the experiment tank, adjustments were made to the mooring line placement angles during the numerical simulation and experimental verification process (Figure 7). Figure 8 shows the schematic of the mooring lines and Tables 3 and 4 illustrate the properties of the mooring lines in the full and model scales for the FOWT platform and FOSS platform. The scaled-down mooring line total lengths for the two platforms were both 14.29 m, the mooring line diameter was 0.32 cm, and the mass per length was 0.21 kg/m; the depth below the still water level to the fairlead was, respectively, 29 cm and 28 cm.

Table 3. Parameters of the mooring lines for FOWT.

Properties of L1, L2, and L3	Full Scale	Model Scale
Number of mooring lines	3×1	3×1
Water depth	100 m	2 m
Line diameter	0.16 m	0.32 cm
Line length	700 m	14.29 m
Unit mass	510 kg/m	0.21 kg/m
Horizontal distance from fairlead to anchor	685 m	14 m
Depth to fairlead below SWL	14 m	29 cm

Table 4. Parameters of the mooring lines for FOSS.

Properties of L4, L5, and L6	Full Scale	Model Scale
Number of mooring lines	3 × 1	3 × 1
Water depth	100 m	2 m
Line diameter	0.16 m	0.32 cm
Line length	700 m	14.29 m
Unit mass	510 kg/m	0.21 kg/m
Horizontal distance from fairlead to anchor	680 m	13.9 m
Depth to fairlead below SWL	13.85 m	28 cm

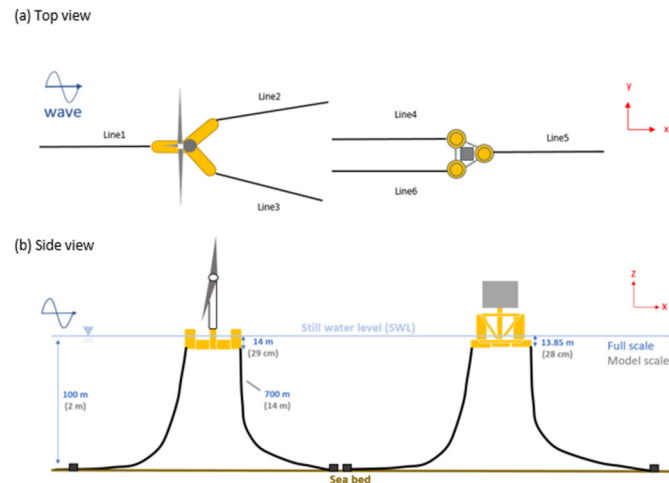


Figure 7. Schematic of the mooring lines.



Figure 8. Photo of mooring lines in model scale.

2.1.4. Dynamic Cable System

Figure 9 shows the cross-section of the cable proposed by Janocha et al. (2024) [20]. Table 5 shows the power cable and buoyancy segment properties proposed by Rentschler et al., 2019 [21], which is the same as Thies et al. (2012) [6]. And the minimum breaking load of the cable is 100 kN. Table 6 illustrates the length configurations of three different forms of fully suspended dynamic cables. The cable shape of the different cases is depicted in Figure 10. Figure 11 depicts the schematic diagram of the dynamic cable model used in this study, with the scaling based on the unit weight in water of the cable segments, buoyancy in the buoyant segment, and bending stiffness. A homogeneous rubber strip material was used for the cable main body, and weights were added by attaching springs. The buoyancy force in the buoyant segment was enhanced with polystyrene balls.

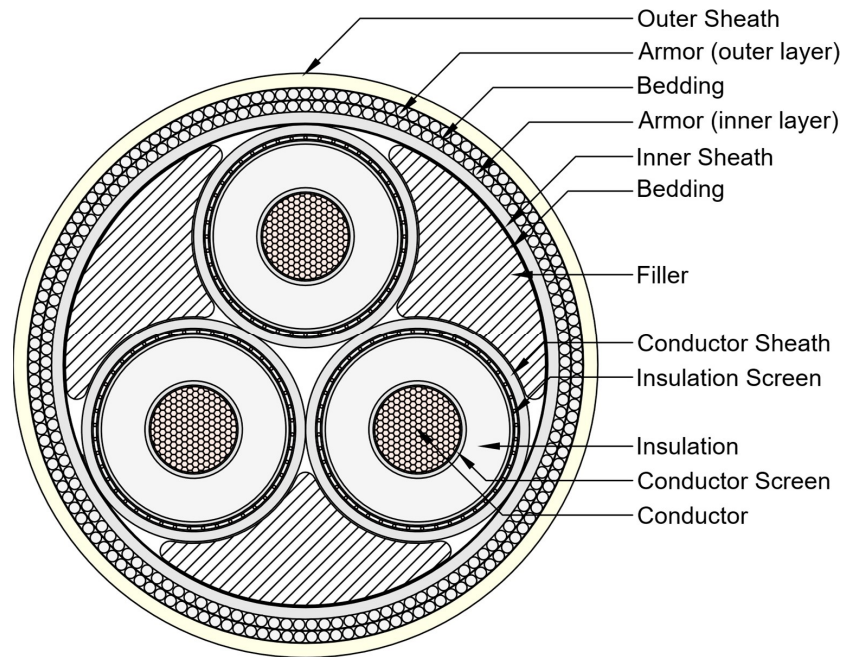


Figure 9. Typical cross-section of a three-phase double-armor power cable (Janocha et al., 2024) [20].

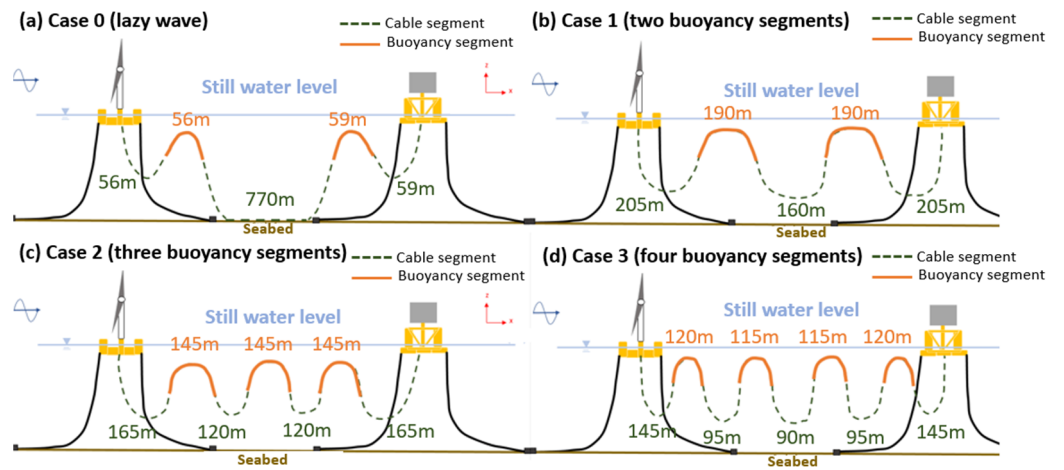


Figure 10. Schematic of the dynamic cable: (a) lazy wave and (b) two, (c) three, and (d) four buoyancy segments.



Figure 11. Dynamic cable experimental model schematic diagram.

Table 5. Parameters of 66 kV dynamic cable.

Properties	Full Scale	Model Scale
Diameter	200 mm	4 mm
Power cable segment unit weight in water	390 N/m	16.6 g/m
Buoyancy segment unit weight in water	−316 N/m	−13 g/m
Bending stiffness	10 kN·m ²	35.4 kN·mm ²

Table 6. Parameters of different schemes.

Properties (Full Scale/Model Scale)	Case 1	Case 2	Case 3
Total length (m)	950/19.4	1005/20.5	1040/21.2
Length of power cable segment (m)	570/11.6	570/11.6	570/11.6
Length of buoyancy segment (m)	380/7.8	435/8.9	470/9.6

2.1.5. The Experimental Measurement Instruments and Methods

The measurement targets of this study include the platform motion response, cable tension, and curvature. The platform displacement measurement method involves using a GoPro for the image analysis and subsequently analyzing the displacement of the two platforms in the surge and heave directions through post-processing. The platform rotation measurement method involves fixing a gyroscope (Figure 12) on the platform and measuring the temporal changes in the platform rotation using a data acquisition system. Because the maximum tension of the dynamic cable occurs at the junction of the connection of the platform and the cable, the tension gauge (Figure 13) connected at the junction of the cable and fairlead can measure the temporal sequence of the cable tension. The cable curvature is selected from positions with significant curvature along the entire cable length. In this study, a cable segment near the wind turbine’s bending section was selected for the cable spot image measurement, and the cable curvature was analyzed through image processing. The detailed experimental configuration diagram is as shown in Figures 14 and 15.



Figure 12. Gyroscope.



Figure 13. Tension gauge.

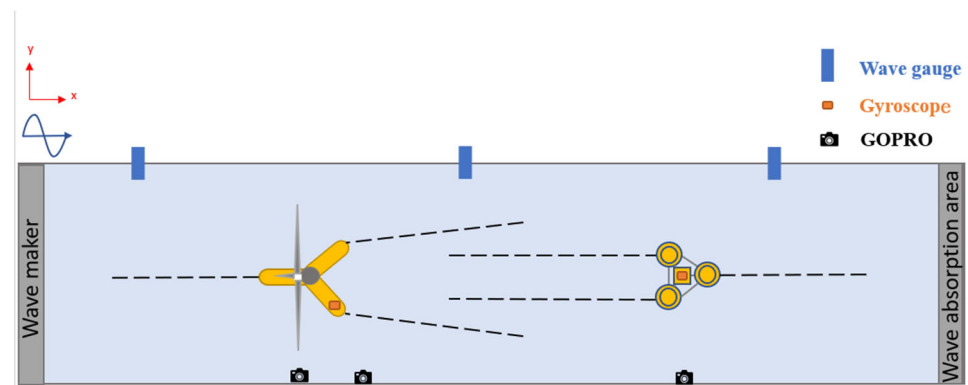


Figure 14. Top view experimental instrument configuration.

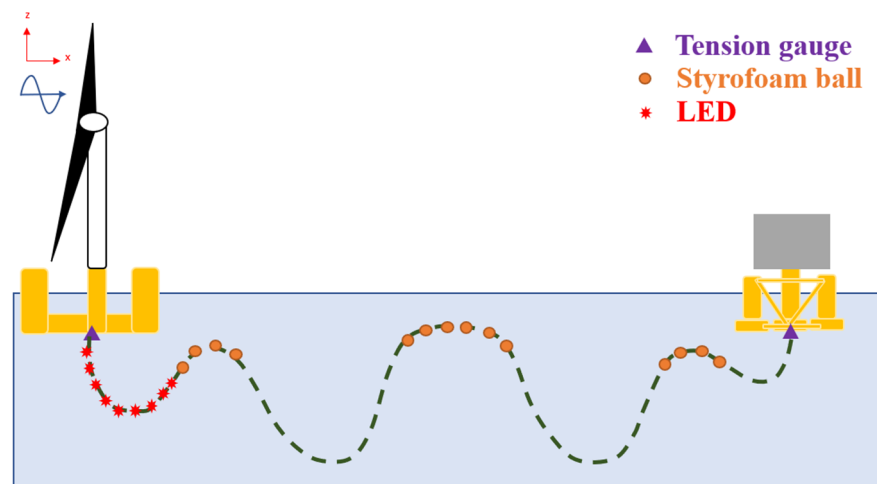


Figure 15. Side view experimental instrument configuration.

3. Numerical and Experimental Validation Results

3.1. Free Decay Test

Free decay involves inducing a particular directional displacement or rotation in the platform and subsequently eliminating external forces. This permits the platform to naturally revert to its equilibrium state by relying on its inherent hydrostatic restoring force and damping effects, resulting in a temporal evolution of the platform’s behavior. The acquired time-series data undergo Fast Fourier Transform (FFT) to derive the energy density within the frequency domain. These data are subsequently employed to identify the resonant period within that specific direction, the results are demonstrated in Figure 16, Tables 7 and 8. This process facilitates the evaluation of both the precision of the numerical simulation platform and the effectiveness of the experimental setup platform.

Compared to the experiments of the FOWT and FOSS platforms, the peaks in the roll and pitch motion were relatively higher in the simulations. This is due to the simulation being based on potential flow theory, which overlooks fluid viscosity and consequently neglects damping effects. However, in the heave motion free decay test, the discrepancy in the model weight resulted in a slightly higher energy peak in the experimental setup compared to the numerical simulation. Finally, this study ensured that the difference in the natural periods between the model and the prototype was less than 10%.

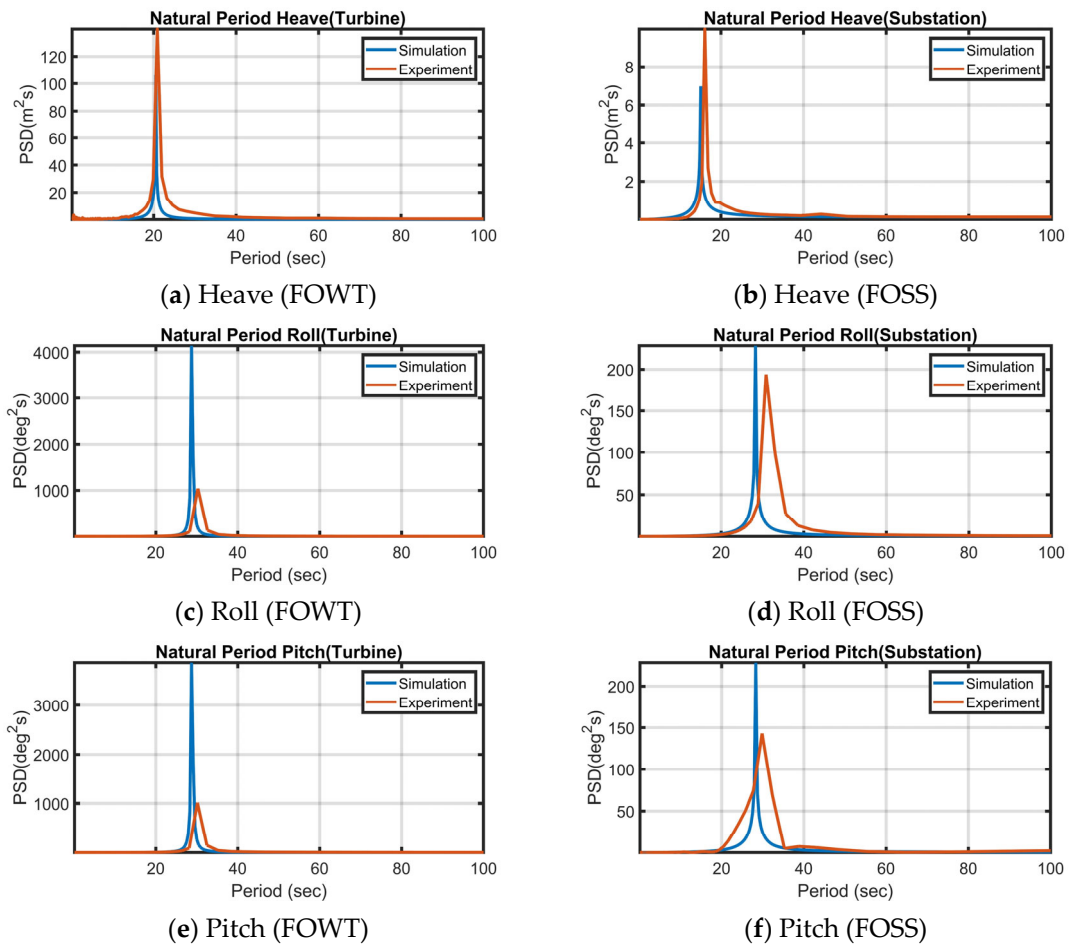


Figure 16. Comparison of natural periods of heave, roll, and pitch of FOWT and FOSS.

Table 7. Comparison of natural periods of FOWT.

Properties	Heave	Roll	Pitch
Simulation	20.5 s	28.7 s	28.7 s
Experiment	20.9 s	30.3 s	30.1 s

Table 8. Comparison of natural periods of FOSS.

Properties	Heave	Roll	Pitch
Simulation	15.1 s	28.3 s	28.3 s
Experiment	16.1 s	30.9 s	29.8 s

3.2. Regular Wave Validation

This section investigates the regular wave validation by keeping the wave height constant and varying the wave period. The regular wave test conditions are presented in Table 9. The Response Amplitude Operator (RAO) was utilized to evaluate the motion responses of the platform and the cable at different periods. This verification aimed to confirm the consistency between the motion responses of the platform under cable tension in both the numerical simulation and experiments. The definition of RAO is as follows:

$$RAO = \frac{A_i}{A_{wave}} \tag{5}$$

where A_i means the amplitude of the investigated physical phenomenon, and A_{wave} means the amplitude of the incident wave.

Table 9. Regular wave test schedule.

Symbols	Wave Height (m)	Wave Period (s)
RH49T08	4.9	8
RH49T11	4.9	11
RH49T14	4.9	14
RH49T17	4.9	17
RH49T20	4.9	20
RH49T22	4.9	22
RH49T24	4.9	24
RH49T26	4.9	26
RH49T28	4.9	28
RH49T30	4.9	30

Figure 17 compares the simulated and experimental RAO results revealing that the surge, heave, and pitch directions for both the FOWT and FOSS platforms exhibit similar trends. Due to the influence of the fluid viscosity and platform damping in the experiments, the results are slightly lower compared to the simulations. Similar trends confirm that the motion responses of the platform in different periods correspond between the simulation and experimentation. However, in the FOSS pitch direction, slight differences in the peak values are observed due to variations in the placement angles and positions of the mooring lines, which lead to discrepancies in restoring the force of the mooring system for the two-dimensional flume experiment.

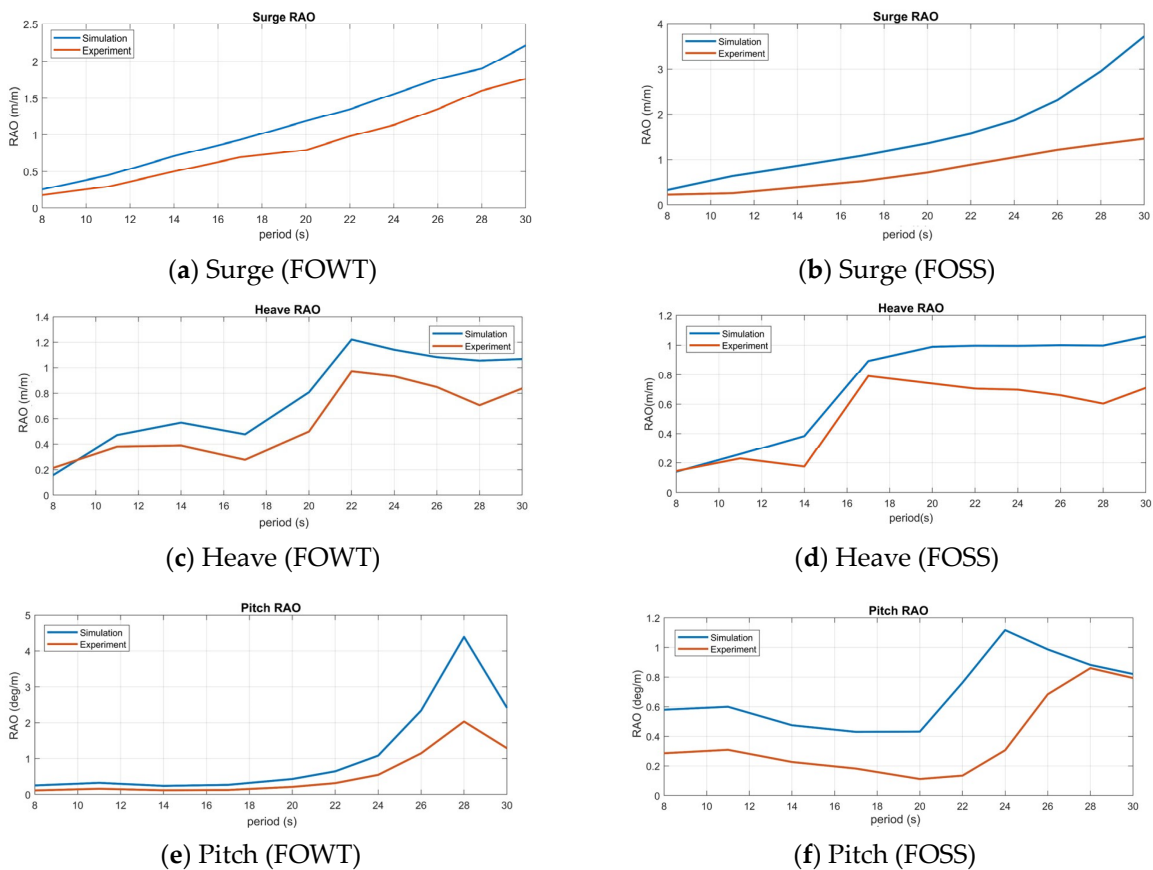


Figure 17. Comparison of the RAO of the surge, heave, and pitch of the FOWT and FOSS.

To validate the trend of dynamic cable tension in the simulations and experiments, this study conducted a tension frequency spectrum validation analysis on the dynamic cable under regular wave conditions. As the maximum tension occurs at the cable–platform connection points, as illustrated in Figure 18, this study focused on discussing those connection points. Connection point A represents the connection between the cable and the FOWT platform, while connection point B represents the connection between the cable and the FOSS platform.

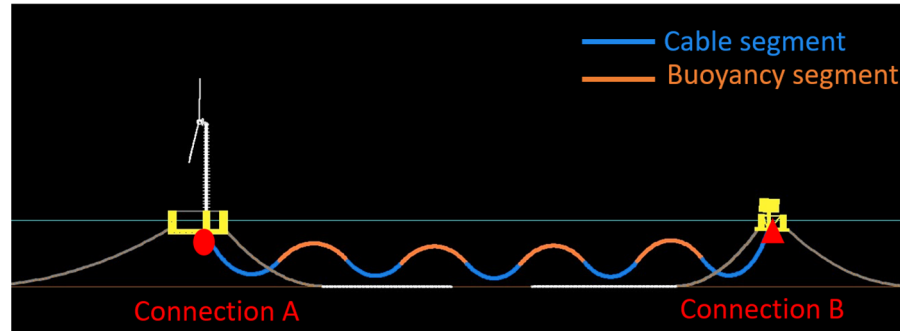
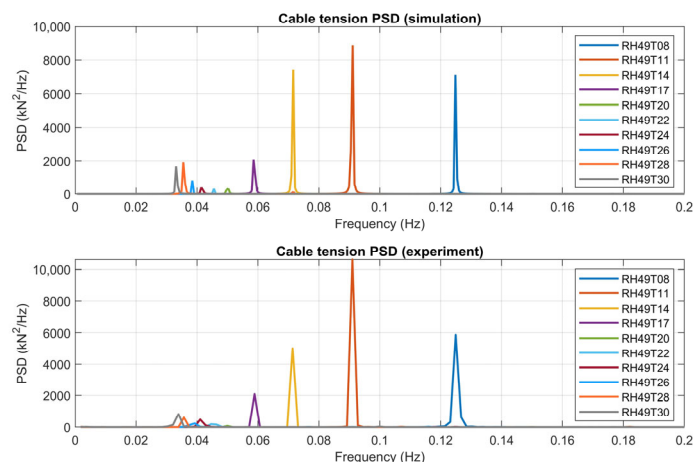


Figure 18. Connection point of dynamic cable systems to validate cable tension.

From the results of Figures 19 and 20, validating the tension frequency spectrum results for the third buoyancy configuration of case 2 and the fourth buoyancy configuration of case 3, it can be observed that the peak frequencies of the different tests in the simulations and experiments are in good agreement, and both align with the wave’s dominant frequency. This verification confirms that the tension performance of the dynamic cable configuration exhibits the same trend in both simulations and experiments.

Because the behavior on both sides is similar, considering the arrangement of the test site, this study conducted the analysis only on the cable bending section near the FOWT platform (section A in Figure 21). Figure 22 shows the measurement of the positions using the image analysis in this study along with the actual images captured by the camera. Figure 23 performs a curvature frequency spectrum analysis on the dynamic cable under regular wave conditions. The maximum curvature of the suspended dynamic cable occurs where the cable bends near the platform.



(a) Connection A (FOWT)

Figure 19. Cont.

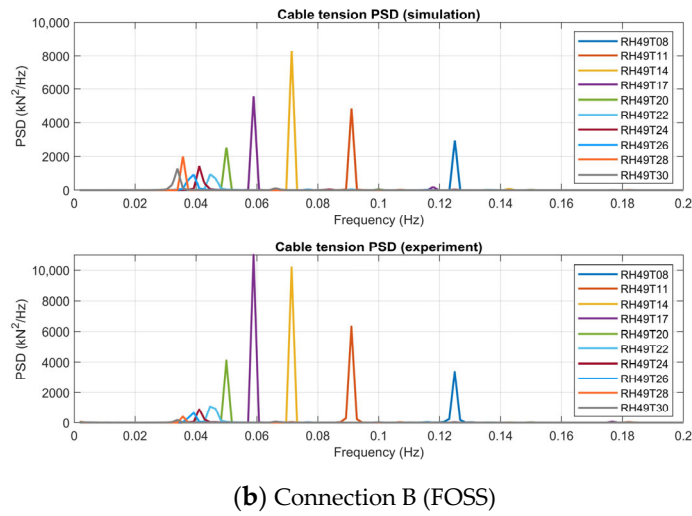


Figure 19. Case 2 dynamic cable tension power spectrum density in regular wave.

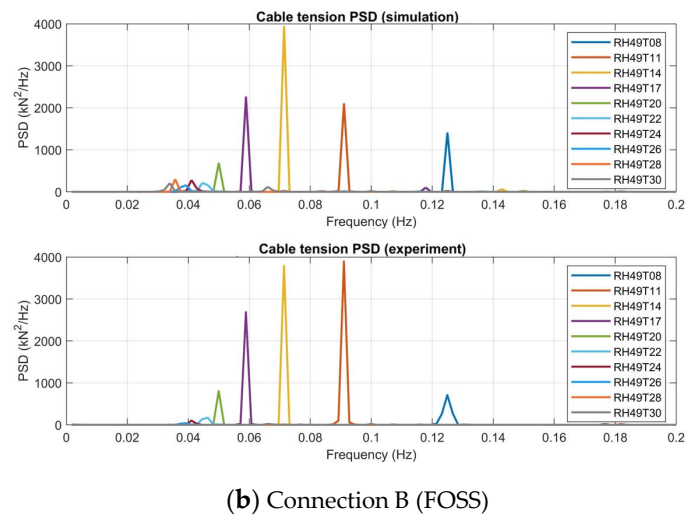
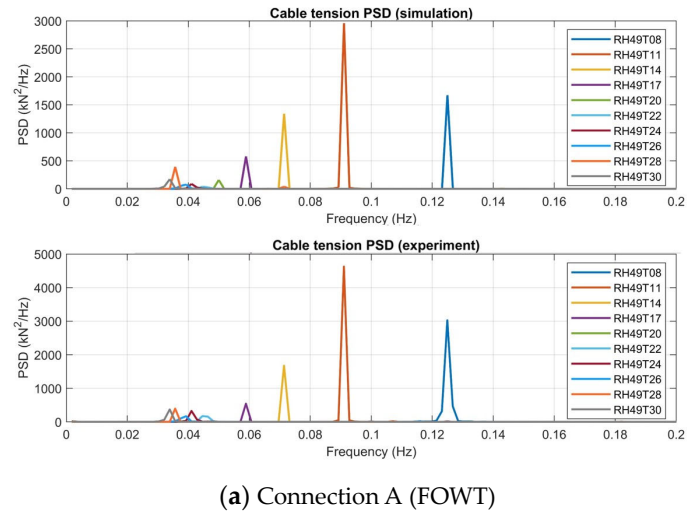


Figure 20. Case 3 dynamic cable tension power spectrum density in regular wave.

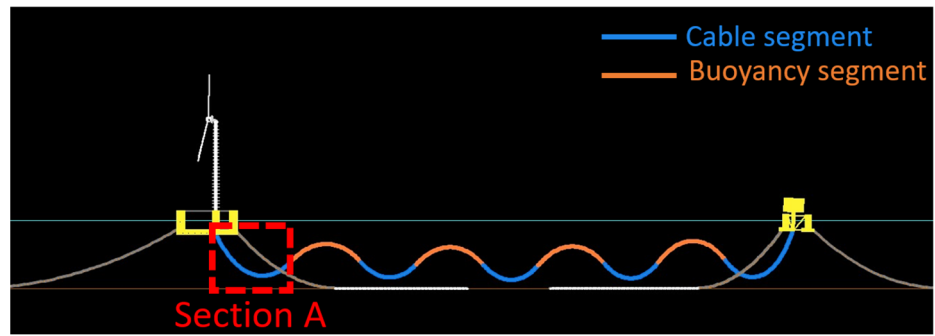


Figure 21. Section of dynamic cable systems to validate cable curvature.

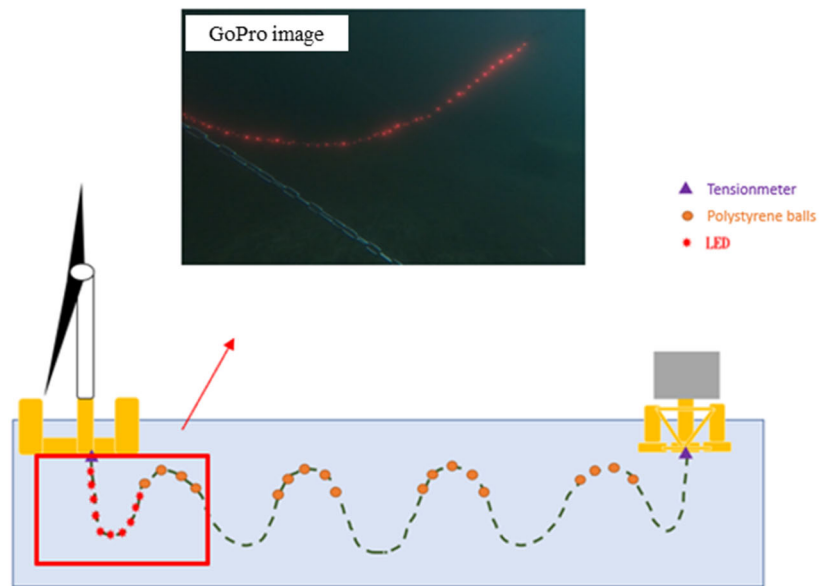


Figure 22. GoPro image of dynamic cable systems in experiment.

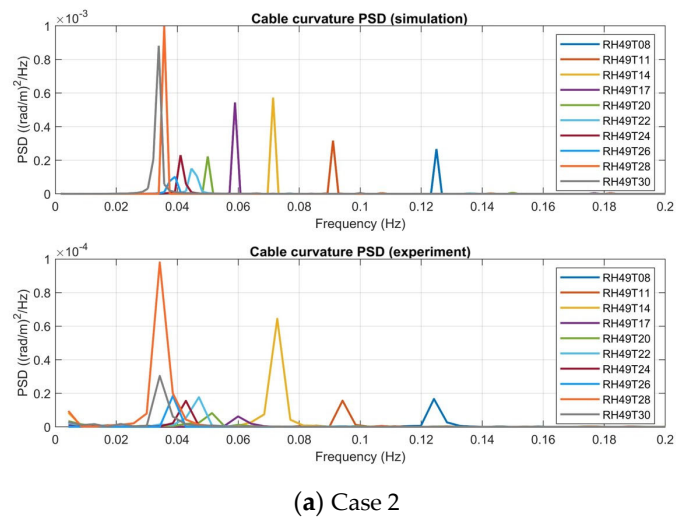


Figure 23. Cont.

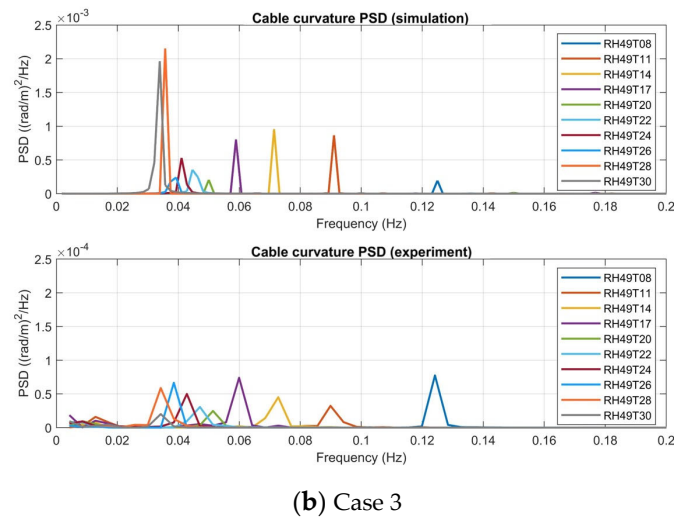


Figure 23. Dynamic cable curvature power spectrum density in regular wave.

3.3. Irregular Wave Validation

In this section, irregular wave verification is conducted, considering the influence of both wave loads and wind loads. The design conditions were based on the ultimate limit state (ULS) for the potential locations, establishing a 50-year return period in the Taiwan Strait. The environmental condition parameters are provided in Table 10. It is noted that the 50-year return period wind speed is 45.6 m/s, and the wind thrust decreases to 456 kN. These values were obtained from OrcaFlex. As shown in Figure 24, the scaled wind thrust at a 1/49 ratio results in 395 g.

Table 10. Fifty-year return period of wind and wave.

Environmental Loads (JH11T13)	Parameters and Values
Wave	H = 11.8 m, T = 13.8 s
Wind speed at hub height	45.6 $\frac{m}{s}$



Figure 24. The 50-year return period wind thrust of the wind turbine model measurement diagram.

Figures 25 and 26 depict the time-series variations in the motion of the FOWT and FOSS during a 50-year return period, the results are listed in Table 11. The initial confirmation of the motion range was conducted using time-series data. After converting the experimental results into field data for comparison, the maximum motion ranges in the surge direction for both platforms show minimal differences between the numerical simulations and experiments of approximately ± 10 m. The pitch angle of the FOWT is approximately within ± 5 degrees, while the rotation angle of the FOSS falls within ± 10 degrees. This preliminary irregular wave verification suggests that the motion performance results in the simulations align closely with those obtained from the experiments.

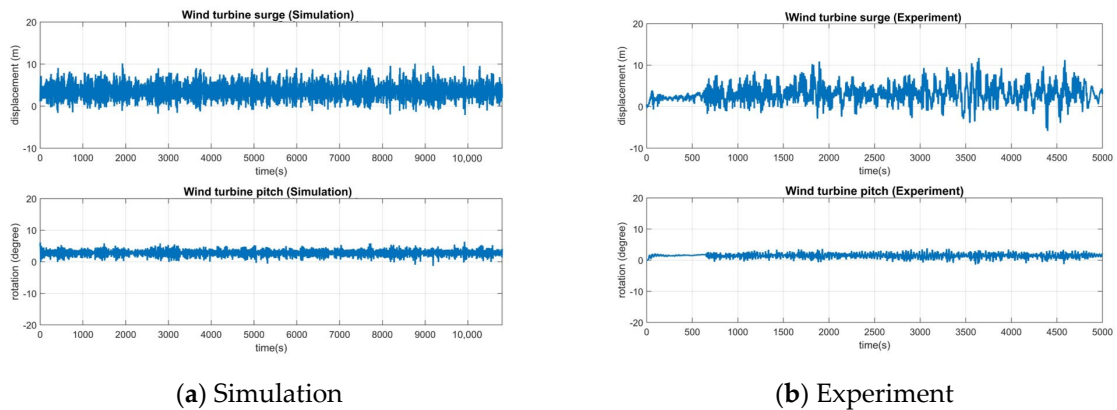


Figure 25. Comparison of FOWT surge and pitch motion between simulation and experiment.

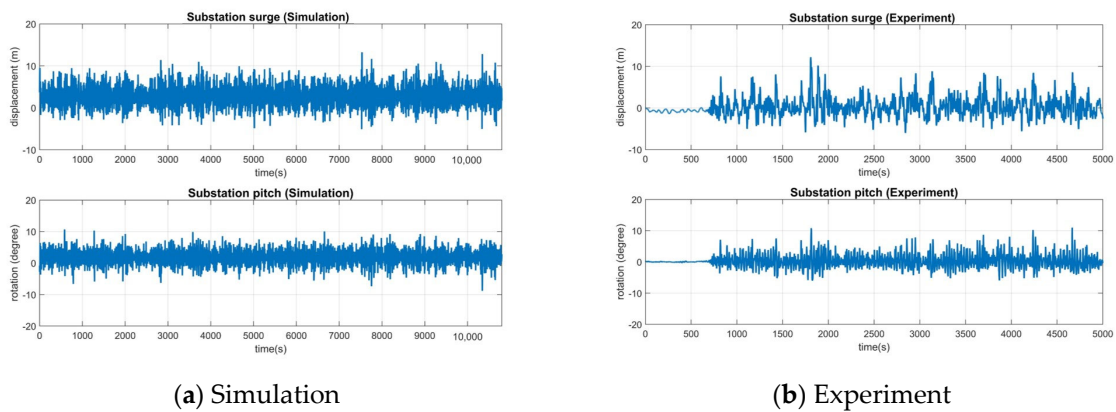


Figure 26. Comparison of FOSS surge and pitch motion between simulation and experiment.

Table 11. Results of surge and pitch motion between simulation and experiment.

	Maximum		Mean		Minimum		Standard Deviation	
	Simulation	Experiment	Simulation	Experiment	Simulation	Experiment	Simulation	Experiment
Surge of FOWT	9.56	11.2	2.9	5.53	-2.8	-6.8	1.83	2.14
Pitch of FOWT	5.9	3.8	2.32	1.45	-1.68	-1.44	0.9	0.7
Surge of FOSS	12.07	11.7	1.08	3.2	-6.95	-7.2	2.37	2.44
Pitch of FOSS	11.24	10.9	1.8	0.25	-9.78	-6	2.41	2.03

The time-series data have been converted into a frequency spectrum for comparison. Figures 27 and 28 show the surge and pitch frequency spectra for the FOWT and FOSS under the 50-year return period wave conditions, respectively. The experimental surge spectrum image analysis was conducted in the interval of 1000 s to 4823 s, with a resampled frequency of 30/7 Hz and 2^{14} data points. The pitch spectrum analysis interval for the experiments was 1000 s to 3294 s, resampled at a frequency of 100/7 Hz, and with 2^{15} data points. The numerical results' spectrum analysis interval was 1000 s to 7554 s, with a sampling frequency of 10 Hz, and both had 2^{16} data points.

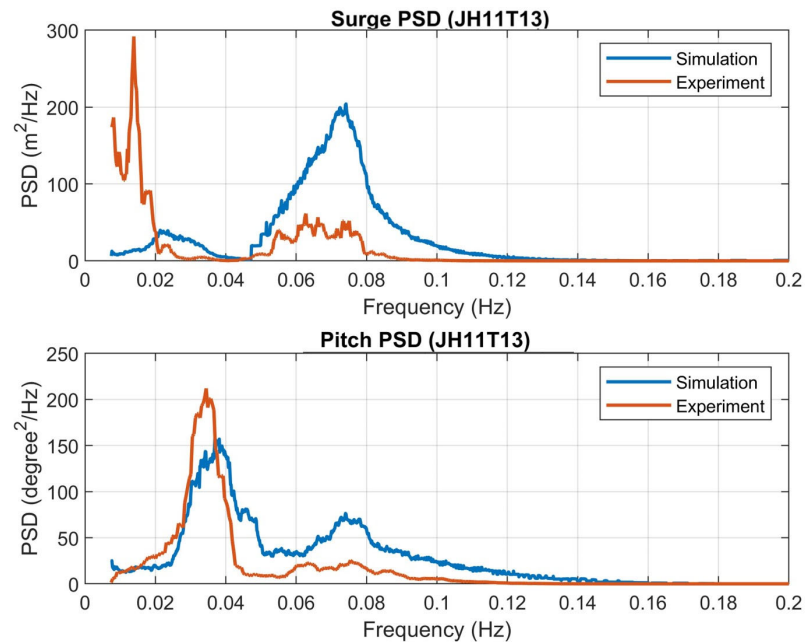


Figure 27. Comparison of FOWT surge and pitch motion power spectrum density between simulation and experiment.

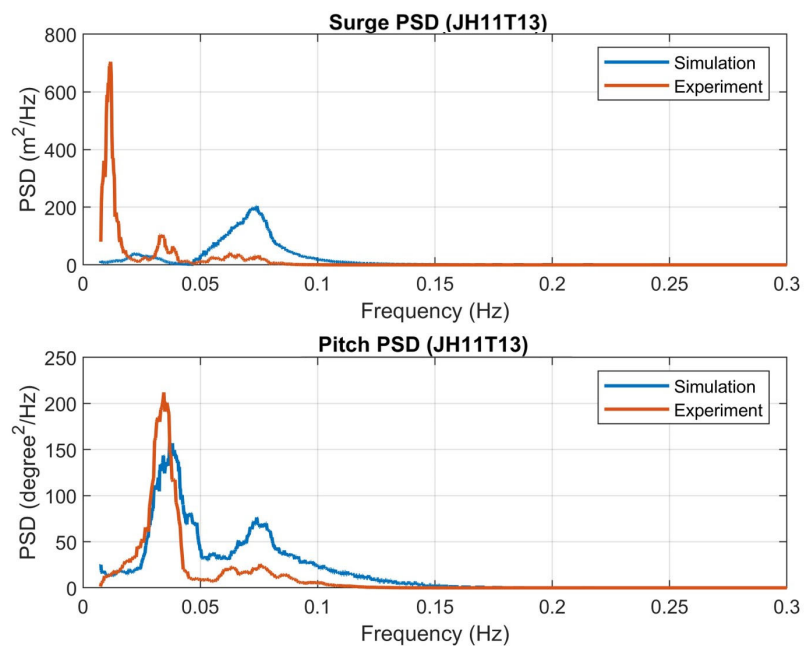


Figure 28. Comparison of FOSS surge and pitch motion power spectrum density between simulation and experiment.

From the result of the power spectrum density, it could be found that energy is concentrated within the dominant frequency range of the waves (0.05–0.1 Hz) in the simulation and experiment of both the FOWT and FOSS surge motion spectra. However, due to the damping effects and fluid viscosity in the experimental setup, the energy within the experimental spectra appears to be comparatively smaller when contrasted with the numerical results. Within the experimental results, a noticeable energy peak emerges in the surge displacement spectrum within the lower frequency range of approximately 0.01 Hz. This phenomenon is attributed to the substantial nonlinear effects of waves, specifically stemming from second-order wave forces, gradual drift motion, and the influence of restoring forces from the anchor system. These factors collectively contribute to a more pronounced spectrum response within the low-frequency range of the experimental floating platform. This enhanced response is a result of the complicated interaction among significant wave nonlinearities.

Furthermore, the interaction between wave and platform nonlinear effects causing wave breaking, as well as the scale effect of the model and mooring lines, can influence the slow drift motion and lead to the low-frequency energy peak of the platforms. Although the numerical simulations in ANSYS AQWA consider wave nonlinear effects to some extent, it remains a frequency-domain analysis and does not directly simulate wave deformations in the time domain. As a result, it does not fully consider wave deformation and its interaction with the floating body. Additionally, the occurrence of wave breaking observed in experiments, as displayed in Figure 29, cannot be modeled accurately in numerical simulations. Therefore, it could be inferred that the calculation of nonlinear effects in the numerical simulations might be smaller compared to the experiments, leading to the smaller energy response of second-order wave forces in the low-frequency spectrum of the numerical simulation.



Figure 29. Wave breaking on FOWT and FOSS platform.

Figures 30 and 31 validate the tension response of the dynamic cable in both the numerical simulations and experiments. This study compared the tension time series at the cable–platform connection point between case 2 and case 3 under the 50-year return period sea conditions. The results indicate that the maximum tension value in the experimental setup slightly exceeded the simulation results after being scaled up to the prototype dimensions. This might be attributed to the lack of consideration of the axial stiffness in the scaled cable model, leading to differences in the tension effects between the stretching and the prototype. It could also be related to the difference in the weight distribution of the dynamic cable, affecting the tension variations. However, it shall be noted that in either case, the maximum tension of the cable does not exceed the minimum breaking load of 100 kN.

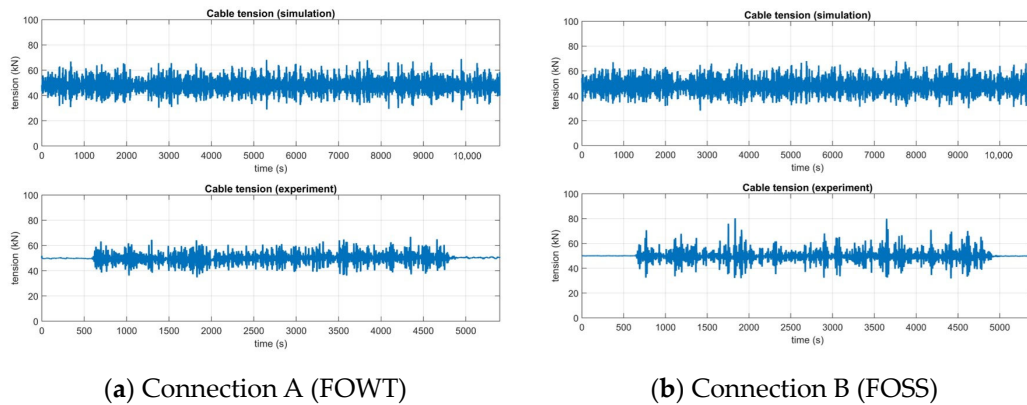


Figure 30. Comparison of dynamic cable tension between simulation and experiment (case 2).

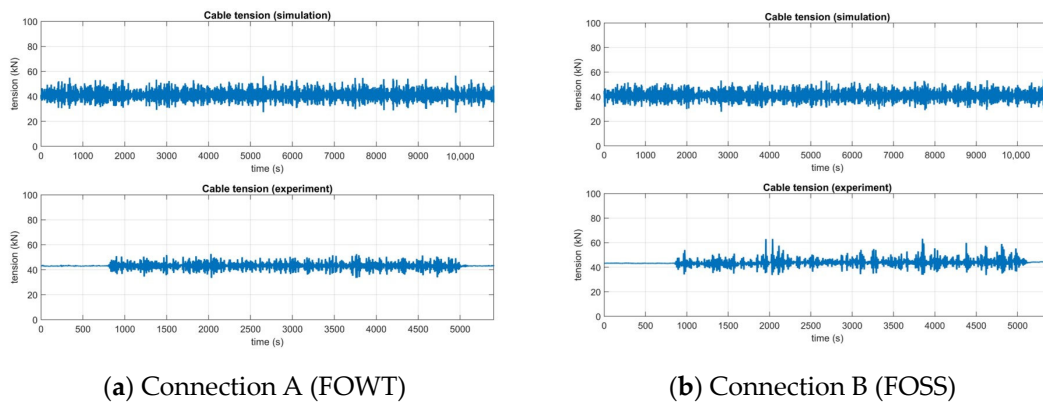


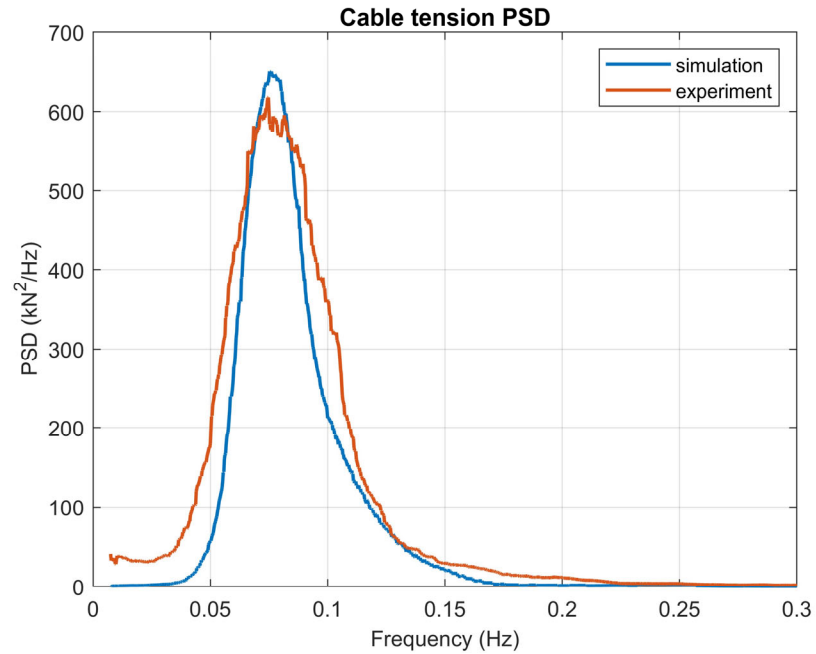
Figure 31. Comparison of dynamic cable tension between simulation and experiment (case 3).

Figures 32 and 33 illustrate the frequency-domain representation of the results obtained from the time-series tension analysis. For the experimental tension spectrum analysis, the time interval ranged from 1000 s to 3294 s. Resampling was carried out at a frequency of 25/7 Hz, resulting in a dataset comprising 2^{13} data points. On the numerical side, the spectrum analysis encompassed a time span from 1000 s to 7554 s, utilizing a sampling frequency of 10 Hz and encompassing 2^{16} data points.

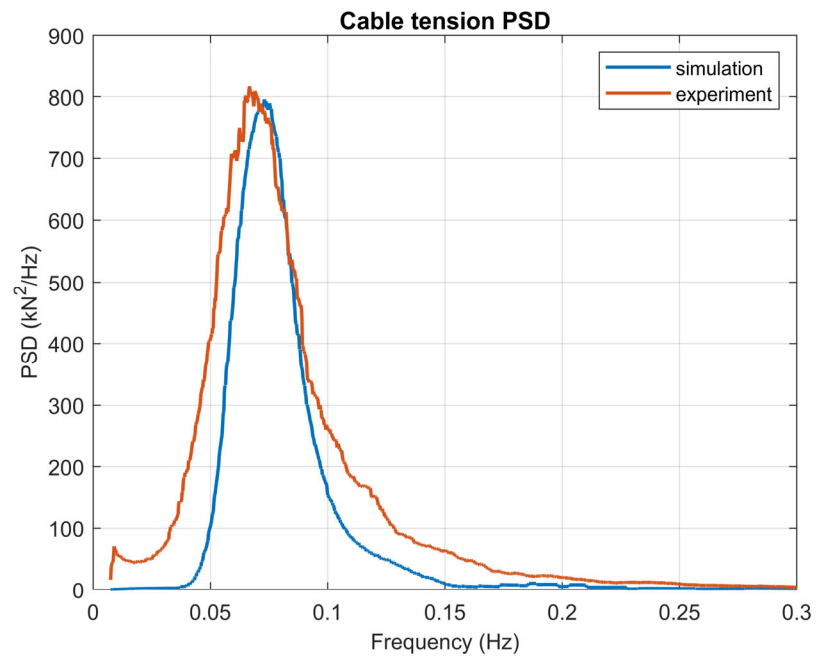
The outcomes uncover a notable correspondence between the energy peaks derived from the simulated dynamic cable tensions and those observed in the experimental dataset, particularly in the scenarios characterized by the 50-year return period wave conditions. These energy peaks consistently align within the frequency range of 0.05–0.1 Hz. Remarkably, these peaks correlate with the dominant frequency of the waves, suggesting that the fluctuations in the dynamic cable tension in both scenarios primarily stem from wave energy influences.

As the time variation in the curvature is relatively small and difficult to observe directly, Figure 34 utilizes a spectral analysis to validate the differences between the simulated and experimental curvature. The analysis range for the experimental spectra is from 1000 s to 4823 s, with a resampled frequency of 7/30 hz and a data point count of 2^{14} ; for the numerical spectra, the analysis range is from 1000 s to 7554 s, with a sampling frequency of 10 Hz and a data point count of 2^{16} . The results indicate that for the 50-year return period, both the experimental and numerical analyses exhibit energy peaks at the main wave frequency, while the differences in the peak values at lower frequencies, as mentioned earlier, may be attributed to second-order wave effects and unexpected motions due to the experimental setup. Furthermore, because the numerical simulation can directly pinpoint the location of maximum curvature, whereas the experimental measurement relies on an image analysis to identify the maximum curvature point along a bent segment, there

might be some positional discrepancy between the experimental and numerical points. Additionally, the inability to measure the two-dimensional curvature accurately in the experiments, as the cable experiences three-dimensional motion, can introduce differences between the experimental and numerical results.

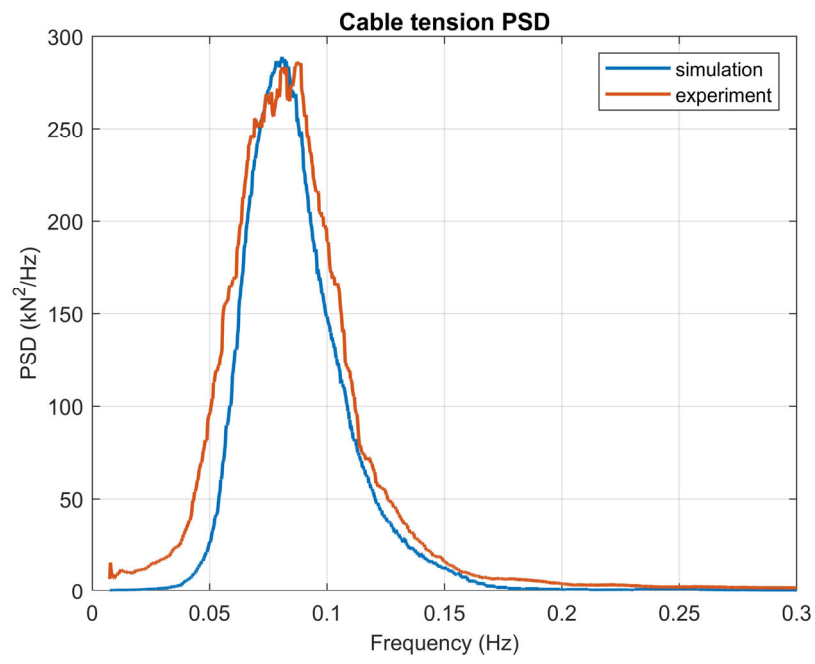


(a) Connection A (FOWT)

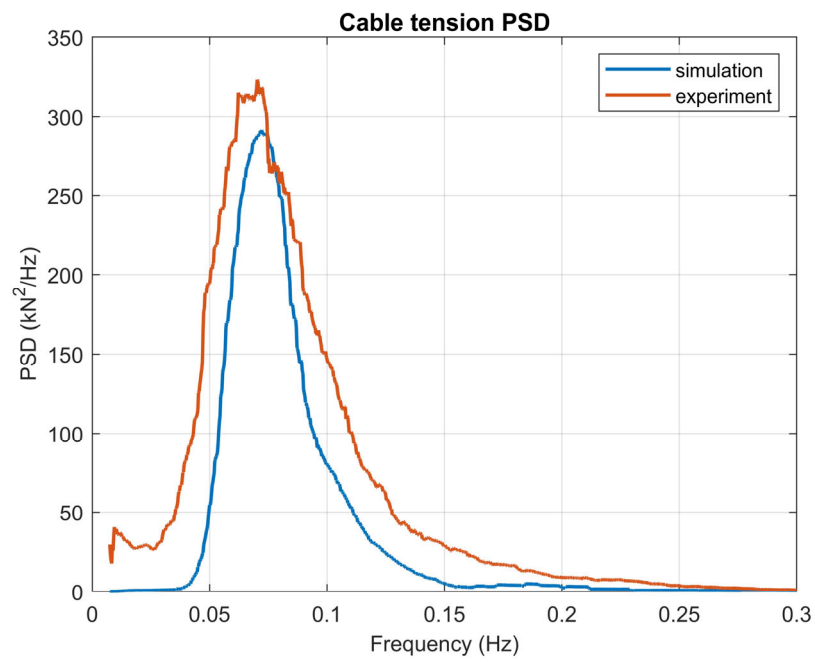


(b) Connection B (FOSS)

Figure 32. Comparison of power spectrum density of dynamic cable tension between simulation and experiment (case 2).



(a) Connection A (FOWT)



(b) Connection B (FOSS)

Figure 33. Comparison of power spectrum density of dynamic cable tension between simulation and experiment (case 3).

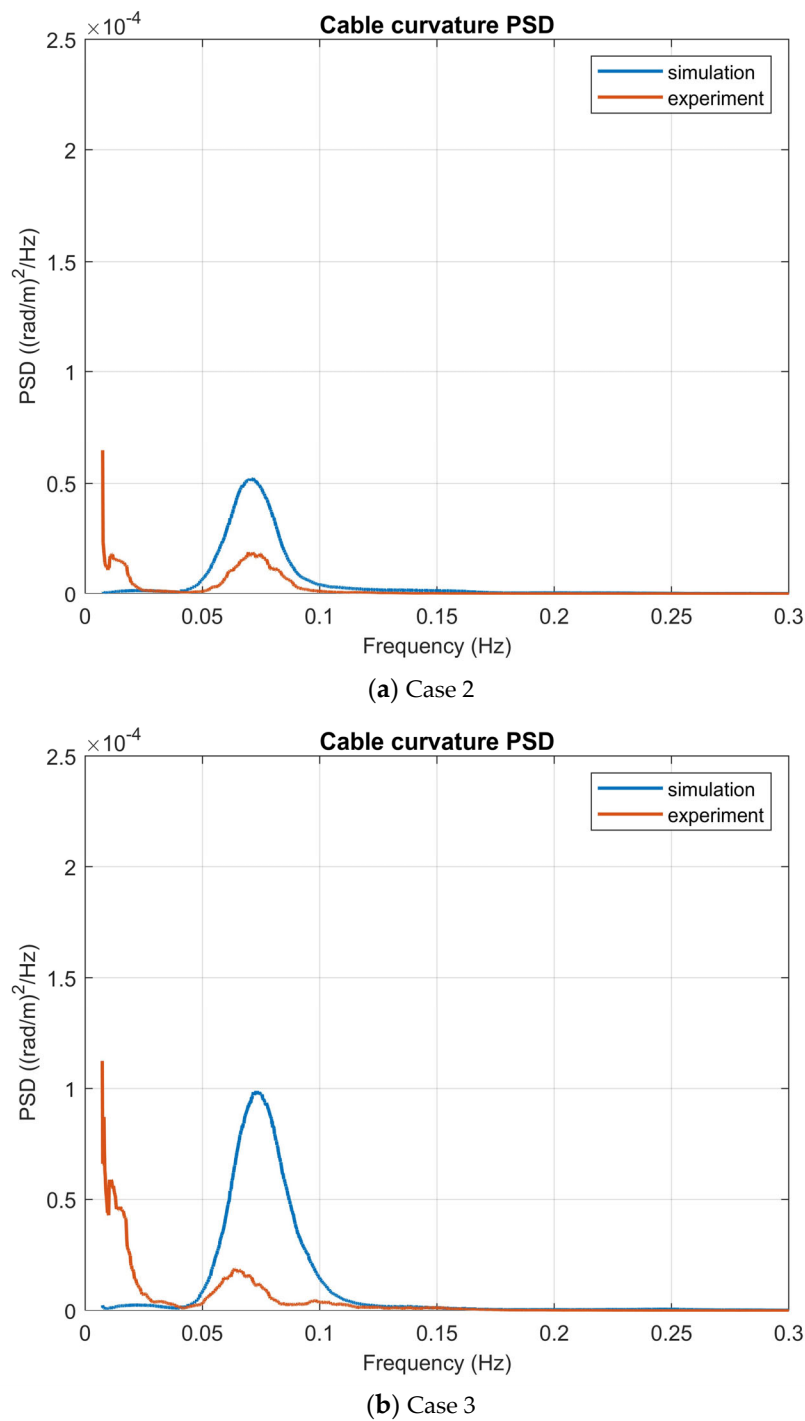


Figure 34. Comparison of power spectrum density of cable curvature between simulation and experiment.

3.4. Brief Summary of Numerical and Experimental Validation Results

The results obtained from the free decay demonstrate that both the floating wind turbine and the floating substation exhibit consistent natural periods, validating the hydrodynamic characteristics of the simulation and experimental platforms. The analysis of the Response Amplitude Operator (RAO) from regular waves reveals that the motion response amplitudes of both platforms follow a similar trend under different wave periods, although the damping effects and fluid viscosity in the experiments tend to be lower than those in the simulations. Consistency is observed in the trends of the tension and curvature RAOs, although the experimental curvature RAOs are lower due to smaller platform RAOs

compared to the simulations, resulting in slight discrepancies in the tension due to the scaling effects in the experiments. The frequency spectra analysis of the cable tension results demonstrates that the peak energies of the cable tension and curvature occur within the same frequency range in both the simulations and experiments.

In the irregular wave analysis, the experimental wave conditions are confirmed to match the numerical simulations. The analysis of the platform motion response, cable tension, and cable curvature in irregular waves shows that the range of platform motion is similar in both the experiments and simulations, with the cable tension tending to be higher in the experiments due to the omission of axial stiffness in the scaled cables. The frequency spectra analysis confirms that the peak energies of the platform motion, cable tension, and cable curvature occur at the same frequencies.

Based on the experimental analysis results, the feasibility of the numerical simulation calculations is validated. Future work will involve numerical simulations based on actual cable configurations on-site and a cable analysis to propose the optimal dynamic cable configuration for suspension.

4. Numerical Model Result and Fitness Assessment

4.1. Verification of Platform and Mooring Line Specifications

This study has selected the Hsinchu offshore area as the target site for its simulation. Considering Taiwan’s susceptibility to typhoons, it is of paramount importance to thoroughly validate the performance of the floating platform, mooring lines, and power cables when subjected to extreme marine conditions in site application. In this section, the mooring configuration differs from the previous one, as it is not restricted by tank adjustments and reflects the actual layout of mooring lines on the floating platforms (Figure 35).

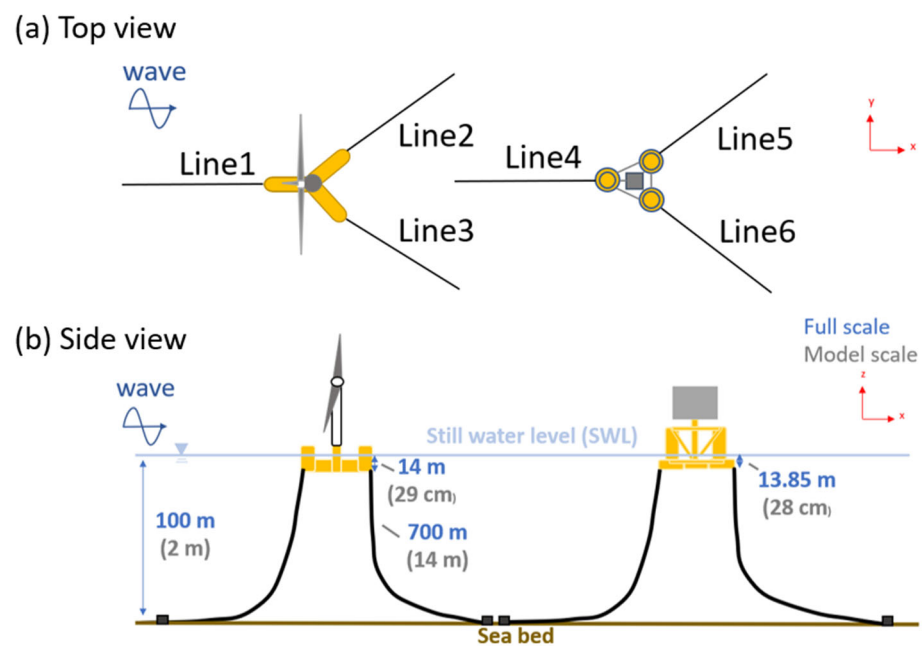


Figure 35. Schematic of the mooring lines in the numerical model.

In accordance with the DNVGL-ST-0119 [22] regulations, it is mandatory to conduct a verification of the ultimate limit state (ULS) wave conditions for the FOWT and FOSS as part of the design criteria. Therefore, this study initially carried out a coupled analysis of the platform and mooring cables to ensure their designs align with the specified regulations under extreme conditions. This verification step is crucial and serves as a prerequisite before delving into the analysis of the physical phenomena associated with the dynamic cable configuration. The parameters of the 50-year return period sea conditions are shown in Table 12. The ULS data in this study respectively refer to the results of the 50-year return

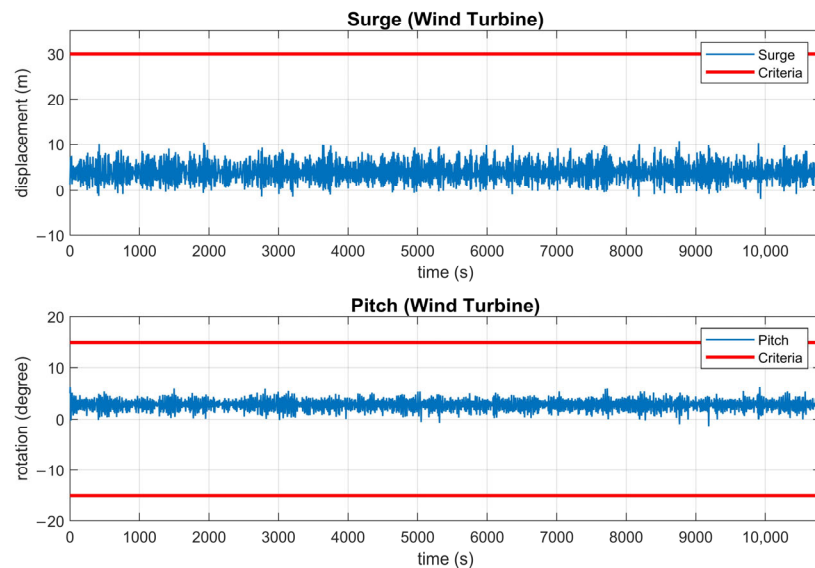
period proposed by Chao et al. (2020) [23] through regression analysis of wave data in Hsinchu, Taiwan. The wind speed data refers to the fifty-year return period data obtained by Chao et al. (2021) [24] through regression analysis of Taiwan offshore wind speed observation tower observation data as the conditions for use. As per the DNVGL-ST-0437 standard [25], the power law formula can be applied to extrapolate the current shear profile if lacking on-site data.

Table 12. Parameters of 50-year return period sea conditions.

Environmental Loads	Parameters and Values
Wave	$H_s = 11.8 \text{ m}$, $T_p = 13.8 \text{ s}$
Wind speed at hub height	$45.6 \frac{\text{m}}{\text{s}}$
Current speed at the sea surface	$0.5 \frac{\text{m}}{\text{s}}$

Following the regulations, this study aims to ensure the structural integrity and safety of the entire system, particularly in the face of extreme weather events, such as typhoons. This robust approach to design and analysis enhances the reliability of floating wind farm systems in challenging marine environments.

Figure 36 illustrates the validation of the mooring lines and the floating platform in alignment with the criteria stipulated in the pertinent international standards. Prior to the subsequent dynamic cable analysis, it was ensured that the mooring design conformed to the standard limits. In compliance with the DNVGL-RP-0286 standards [26] and the guidance outlined in the COREWIND D2.1 (Ikhennicheu et al., 2020) [5] report, for FOWTs operating in severe environmental conditions, it is imperative that the drift of platform range remains within 30 m in 100 m water depth, and the platform rotation does not exceed 15 degrees. The results confirm that the motion responses of both floating platforms meet the criteria outlined in the standards.



(a) FOWT

Figure 36. Cont.

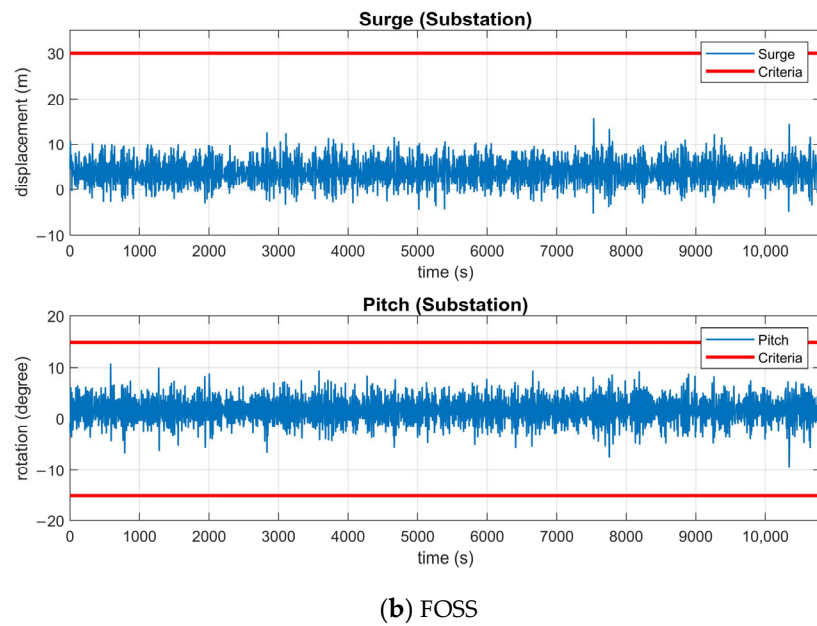


Figure 36. FOWT and FOSS platform motion in 50-year return period loadings.

The verification of the mooring lines is conducted in accordance with the DNVGL-OS-E301 standard [27], which specifies that the maximum tension in the mooring lines under extreme conditions must not exceed 0.95 times the minimum breaking load. Therefore, the mooring lines are inspected based on the criteria outlined in the mentioned standard. Figure 37 illustrates that the cable design has passed the compliance check according to the standards.

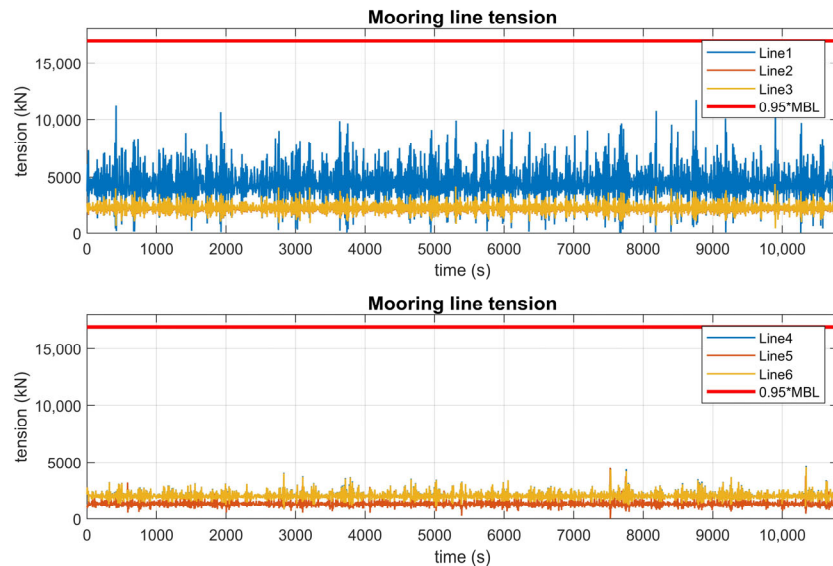
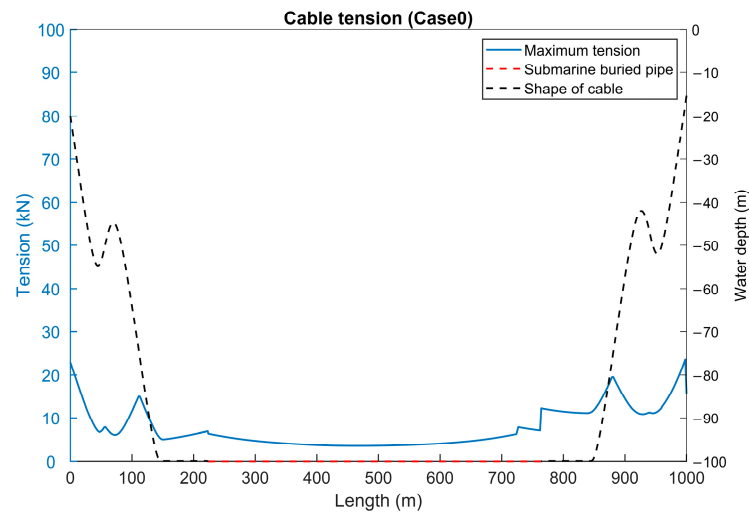


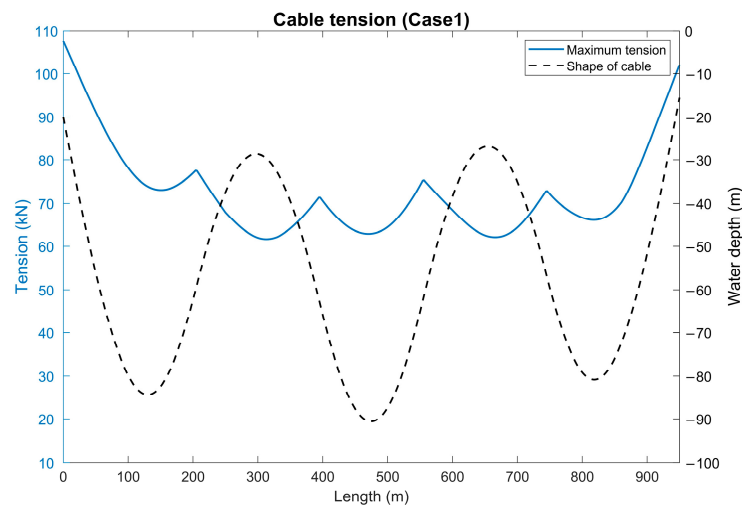
Figure 37. Mooring lines tension in 50-year return period wave conditions.

4.2. Analysis of Dynamic Cables

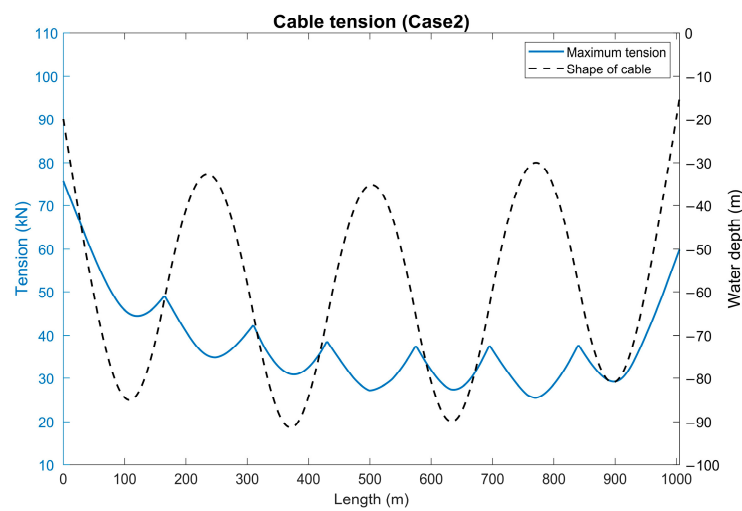
Figure 38 depicts the cable tension distribution under extreme sea conditions with a 50-year return period of wind, wave, and current. The results show that in both the lazy wave and suspended dynamic cable configurations, the maximum cable tension occurs at the connection points. Therefore, when designing the cable, protective measures can be taken at these connection point locations.



(a) Case 0

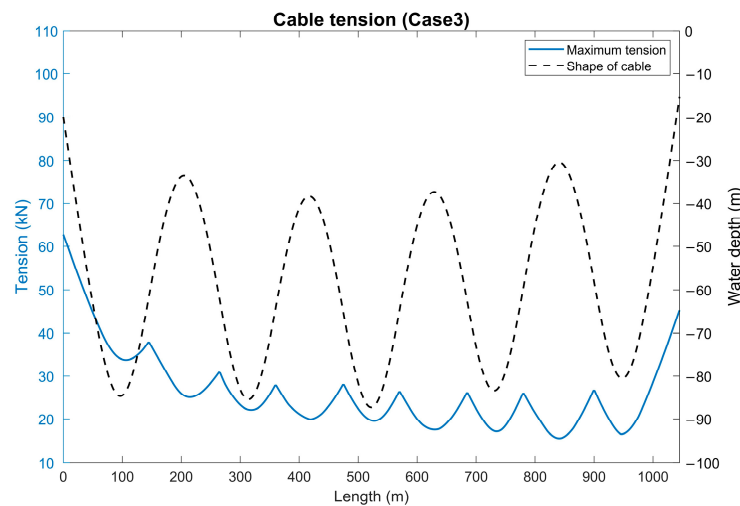


(b) Case 1



(c) Case 2

Figure 38. Cont.



(d) Case 3

Figure 38. Maximum tension distribution of power cables.

According to the results, the cable tension of case 1 with two buoyancy segments at the cable–wind turbine connection point exceeds the minimum breaking load of the cable (100 kN). Therefore, the configuration cannot survive in extreme sea conditions and cannot be used in the Taiwan Hsinchu sea areas. In general, by comparing the tension in the three suspended cable configurations, with the cable segment length fixed, increasing the number of buoyancy modules effectively reduces the average cable tension along the entire cable.

The cable material itself has a curvature limit, and in this study, the maximum allowable curvature for the cable is set to be 0.5 rad/m. Therefore, the analysis focuses on determining the maximum curvature of the cable under extreme conditions. The results in Figure 39 show that in all the suspended dynamic cable configurations designed in this study, the maximum cable curvature under extreme conditions is less than that of the lazy wave configuration. Due to the influence of waves and ocean currents, the shape of the suspended dynamic cable can deform as it experiences displacement, leading to larger curvatures near the FOSS where the cable is more prone to compression.

Figure 40 indicates the minimum distance between the suspended dynamic cable configuration and the water surface to assess the navigational depth available for ships under normal sea conditions. The analysis is conducted under the normal sea conditions provided in Table 13. For the same cable segment length, increasing the buoyancy segments allows the suspended dynamic cable to be deployed in deeper waters. This not only reduces the impact of higher surface velocities on the cable but also provides deeper draft clearance for passing ships.

Table 13. Parameters of normal sea conditions.

Environmental Loads	Parameters and Values
Wave	$H_s = 1.5 \text{ m}$, $T_p = 6.8 \text{ s}$
Wind speed at hub height	$25 \frac{\text{m}}{\text{s}}$
Current speed at the water surface	$0.5 \frac{\text{m}}{\text{s}}$

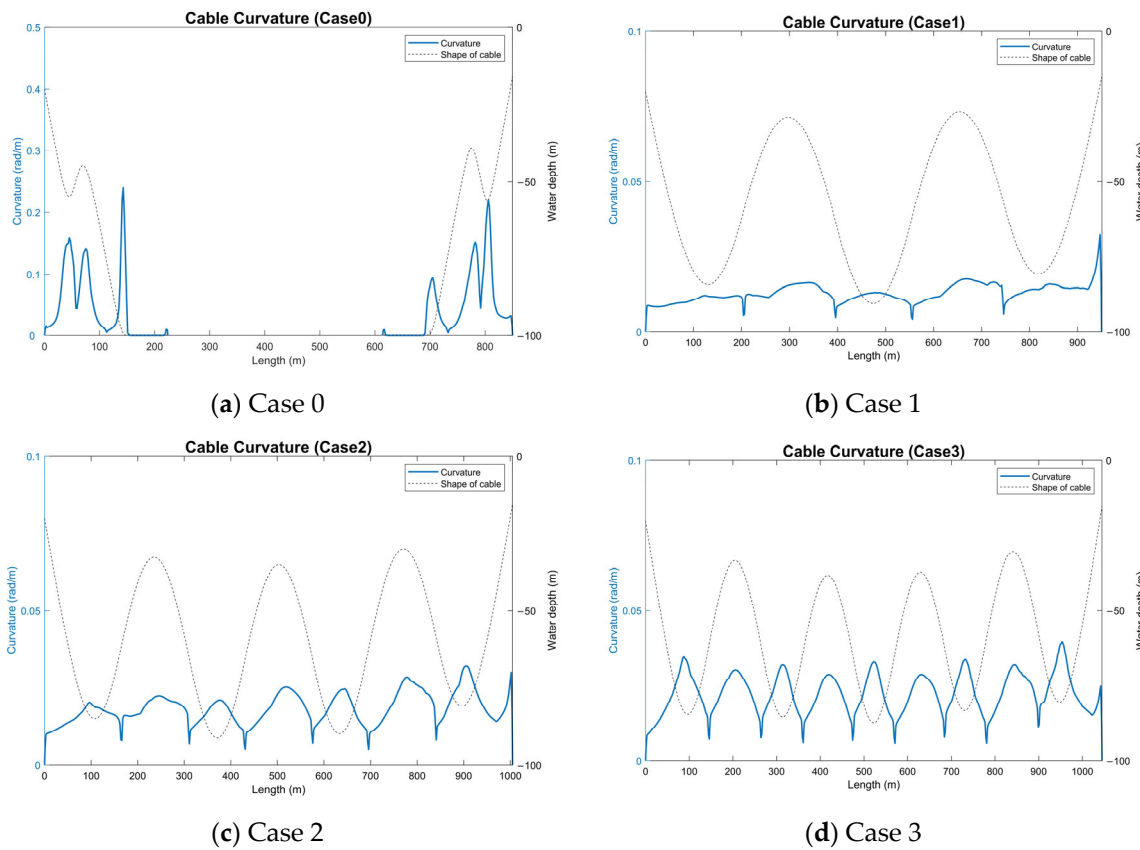


Figure 39. Maximum curvature distribution of power cables.

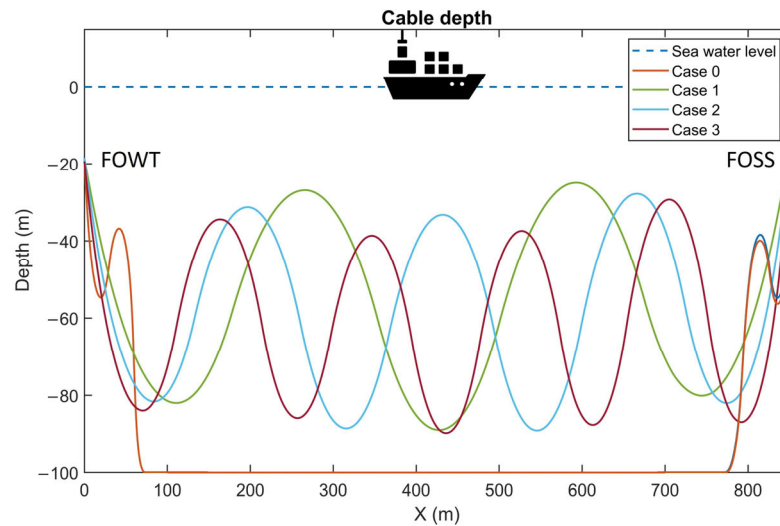


Figure 40. The depth at which the cable is submerged underwater on the seabed.

The submarine cable material consists not only of pure metal but also includes various materials, such as polyethylene. In addition to experiencing damage from repeated loading, dynamic cables can also suffer damage from repeated bending due to long-term environmental loads. Therefore, using S-N curve calculations for fatigue damage may not be suitable. In this study, referencing Sobhania et al. (2020) [7], the method for calculating the fatigue damage of dynamic cables involves assuming the dynamic cable as a homogeneous copper conductor for calculation purposes. The strain-life (ϵ -N) curve is used to calculate the number of strains. The strain of the cable is converted using equations, transforming

the time series of the cable tension and curvature into a time series of strain. The equation representation is as follows:

$$\epsilon(t) = \frac{N(t)}{A} + \chi(t) \cdot E \cdot \frac{D}{2} \tag{6}$$

$\epsilon(t)$ represents the strain time series, $N(t)$ represents the cable tension time series, A is the cross-sectional area, $\chi(t)$ represents the curvature time series, and E is Young’s modulus.

The strain–life (ϵ - N) curve utilizes the copper strain–life curve proposed by Karlsen et al. (2009) [28] for the calculation. The strain–life curve of copper material includes both elastic and plastic strains, and the equation for the total strain range can be expressed as the following equation.

$$\epsilon_{a,total} = \epsilon_{a,pl} + \epsilon_{a,el} = C_1 N^{-\beta_1} + C_2 N^{-\beta_2} \tag{7}$$

$C_1 = 0.7692$, $C_2 = 0.0219$, $\beta_1 = 0.5879$, and $\beta_2 = 0.1745$.

The rainflow method is employed to calculate the fatigue damage value under a single environmental condition. Subsequently, considering the probability of each sea condition occurrence, these values are accumulated using Miner’s rule (Miner, 1945) [29] to determine the cable cumulative fatigue damage over one year.

In this study, a statistical approach has been applied to compile the fatigue environmental conditions, referencing Konispoliatis et al. (2022) [30]. This research collected data from the Hsinchu Buoy (120.84° E, 24.76° N), which was made available by the Central Weather Administration (CWA), Taiwan, covering the years from 2010 to 2021. This dataset encompassed a substantial total of 9,359,234 entries. To facilitate our calculations, the median values were chosen to represent significant wave heights. Following this, the weighted calculations were applied to determine the representative wave periods corresponding to the different significant wave heights. These derived values were subsequently employed as the wave conditions for the fatigue analysis in Table 14.

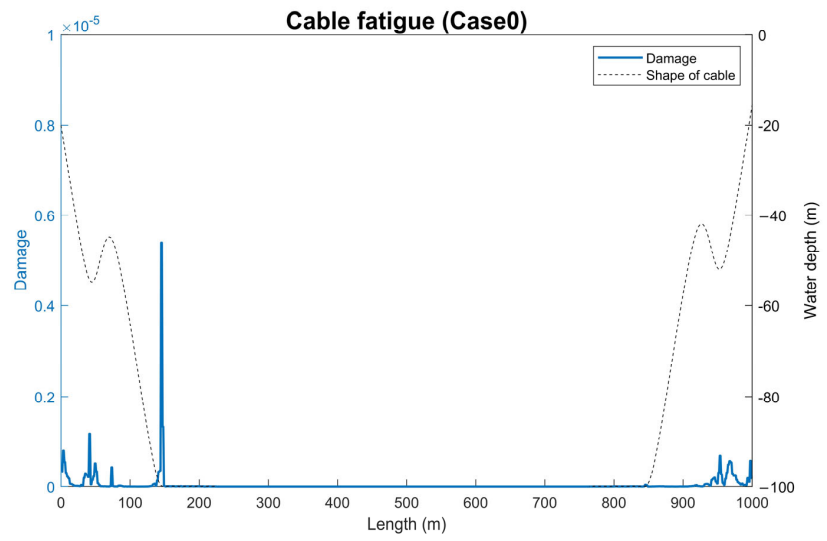
Table 14. Parameters of fatigue analysis sea conditions.

Sea State	Wave Height (m)	Wave Period (s)	Current Speed at Sea Surface (m/s)	Wind Speed at 10 m Height (m/s)	Probability (%)
1	0.5	5.51	0.5	7.653	32.1
2	1.5	6.8	0.5	7.653	46.05
3	2.5	7.95	0.5	7.653	19.15
4	3.5	8.8	0.5	7.653	2.42
5	4.5	9.72	0.5	7.653	0.18
6	5.5	8.71	0.5	27.63	0.03
7	6.5	9.24	0.5	27.63	0.03
8	7.5	9.5	0.5	27.63	0.02
9	8.5	9.5	0.5	29.35	0.01
10	9.5	9.5	0.5	29.35	0.01

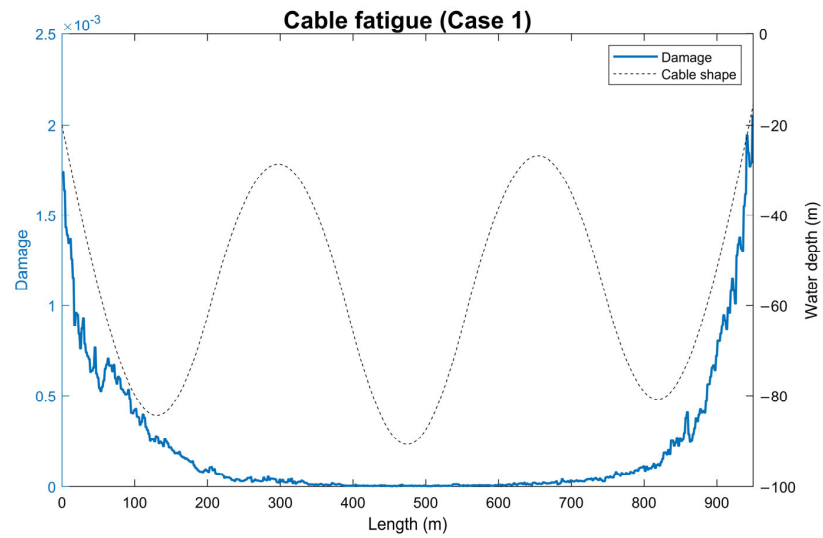
Figure 41a illustrates that in the lazy wave configuration, the cable fatigue damage primarily accumulates in the sag and touchdown zones. This corresponds to the curvature distribution in this configuration, which shows higher curvature values. It indicates that in the lazy wave configuration, the cable fatigue accumulation is mainly influenced by the curvature.

Figure 41b–d explain that in the suspended dynamic cable configuration, the cable fatigue damage mainly accumulates at the cable connection points. This corresponds to the higher tension distribution in this configuration. Therefore, in the suspended cable configuration, the cable fatigue damage is primarily driven by tension.

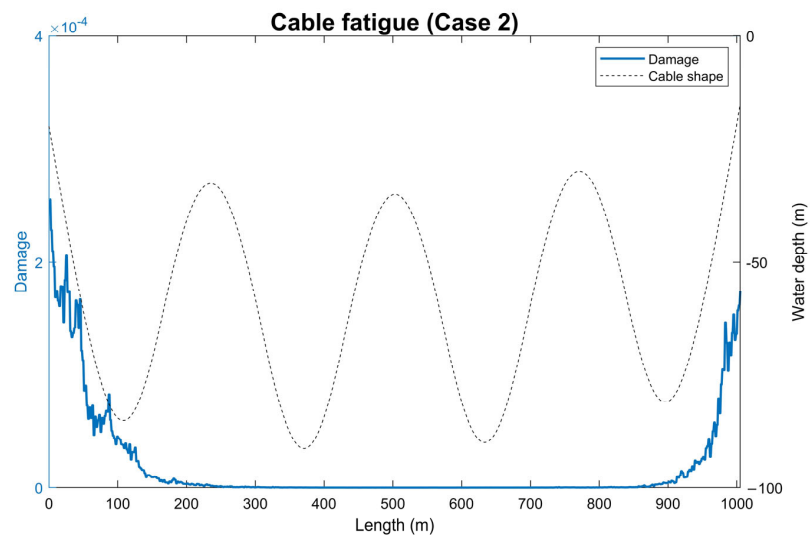
Based on the overall fatigue analysis results and without considering factors like marine growth, the suspended dynamic cable configuration can survive under the operating cycle of the wind turbine.



(a) Case 0



(b) Case 1



(c) Case 2

Figure 41. Cont.

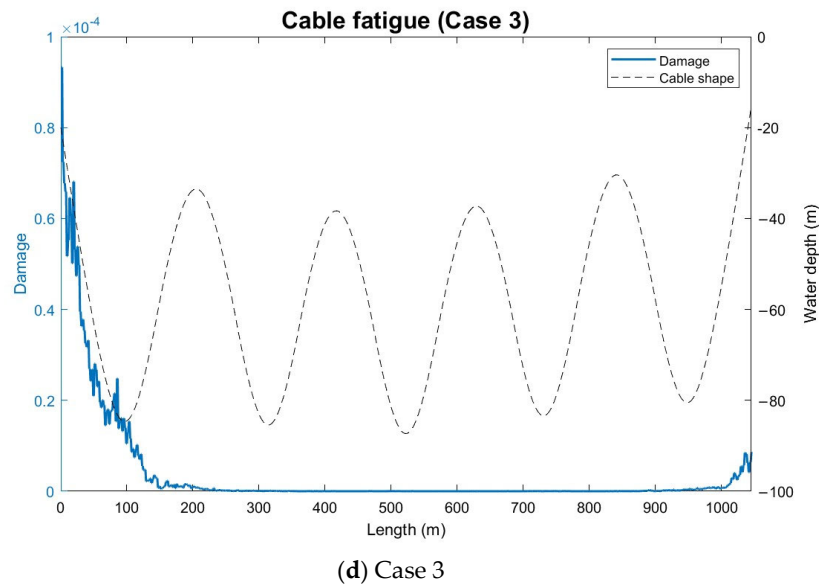


Figure 41. The distribution of cable fatigue damage.

4.3. Analysis of Dynamic Cables

The purpose of this study is to design a suspended dynamic cable configuration suitable for use in the Taiwan offshore area. To compare the suitability of different configurations, this study references the relevant research by Rentschler et al. (2019) [21] and conducts an analysis of dynamic cable systems using two sets of normalized ratio parameters summed as the fitness parameter. This assessment is aimed at evaluating the suitability of different cable configurations, where lower fitness parameter values indicate a better fit for the designed conditions. The equation is defined as follows:

$$Fitness = \frac{T_{max}}{MBL} + \frac{\rho_{max}}{MAC} \tag{8}$$

where T_{max} is the maximum tension and ρ_{max} is the maximum curvature during the simulation, MBL is the minimum breaking load of the cable, and MAC is for the maximum allowable curvature.

The fitness parameters can be adjusted based on the specific focus and evaluation requirements of the study, such as cable fatigue, cost considerations, and more. In this study, in addition to the tension and curvature parameters, the cable fatigue and cable submerged depth are included in the assessment to compare and evaluate the suitability of different schemes for the Taiwan Hsinchu offshore area. The equation is defined as follows:

$$Fitness = \frac{T_{max}}{MBL} + \frac{\rho_{max}}{MAC} + \frac{Water\ depth - submerged\ depth}{Water\ depth} + \frac{Damage_{max}}{fatigue\ failure} \tag{9}$$

where the submerged depth is the minimum distance from the sea surface to the cable, and $Damage_{max}$ is the maximum fatigue damage of the cable. The water depth in this research is 100 m, and the fatigue failure of the cable is 1.

Based on the results of each normalized parameter listed in Tables 15 and 16, it can be observed that the suspended cable configuration, which suspends the entire cable, performs better compared to the lazy wave configuration with a higher curvature. On the other hand, the lazy wave configuration, with a touchdown point, can effectively resist the weight of the cable, reducing the tension at the cable connection point. Therefore, in terms of normalized tension, the lazy wave configuration outperforms the suspended configuration.

Table 15. Simulation results for different cable configurations.

Properties of Power Cable	Case 0	Case 1	Case 2	Case 3
Maximum tension (kN)	24.02	107.51	75.7	62.73
Maximum curvature (rad/m)	0.241	0.032	0.032	0.054
Submerged depth (m)	42.52	26.27	29.68	30.91
Fatigue damage	5.4×10^{-6}	2.1×10^{-3}	2.55×10^{-4}	9.33×10^{-5}

Table 16. Normalized parameters for different cable configurations.

Properties of Power Cable	Case 0	Case 1	Case 2	Case 3
Maximum tension (kN)	0.24	1.08	0.76	0.63
Maximum curvature (rad/m)	0.48	0.06	0.06	0.11
Submerged depth (m)	0.57	0.74	0.70	0.69
Fatigue damage	5.4×10^{-6}	2.1×10^{-3}	2.55×10^{-4}	9.33×10^{-5}
Fitness	0.24	1.08	0.76	0.63

Furthermore, in the suspended configuration, case 3 demonstrates superior performance compared to cases 1 and 2 across various metrics, including the tension, curvature, submerged depth, and annual fatigue damage. Notably, it also exhibits a similar fitness level as the lazy wave configuration. Consequently, when assessed using the fitness parameters, the four buoyancy segment configuration developed in this study is deemed the optimal suspended dynamic cable configuration that can be used in Taiwan Hsinchu sea areas.

This finding emphasizes the importance of meticulous buoyancy segment design, especially when considering different platform spacings and cable lengths. This attention to detail is vital to ensure suitability for deployment in various sea conditions across different marine regions. Such optimized designs are essential for improving the reliability and efficiency of floating structures, as examined in this study.

5. Conclusions and Future Works

In this study, the suspended dynamic cable motion response between the FOWT and FOSS was simulated. The experimental results of the cable behavior in the wave responses were compared by using two commercial codes (AQWA and OrcaFlex) with model tests. Some conclusions and recommendations for future work are as follows.

The free decay tests indicate that the model with six-degrees-of-freedom (6DOFs) natural periods closely matched its prototype. In both the numerical simulations and model tests, the verification results for regular waves show good consistency in the Response Amplitude Operator (RAO) of the platform motion, cable tension, and cable curvature. The frequency spectrum analysis indicates that the energy peaks of these parameters are close to the wave’s main frequency, indicating that there is significant influence from the waves. Moreover, the energy peak frequencies in the numerical results align with those in the experimental results.

For irregular wave verification, there is consistency in the trend of the platform motion range, demonstrating that the platform computation and experimental model share similar characteristics. The cable tension results show good consistency in the frequency spectrum but slight differences in the time-series comparison, primarily due to the neglected influence of axial stiffness caused by model scaling. However, the evaluation under extreme sea conditions indicates that the fully suspended cable configuration can effectively reduce tension values under extreme conditions. Nevertheless, Scheme One fails to meet the minimum breaking force requirement under specific sea conditions.

Upon completion of the validation, the numerical results, which considered the actual cable performance in the operating phase, cable tension, cable curvature, submerged depth, and fatigue damage, were simultaneously compared based on the fitness parameters. Further analysis reveals that the floating configuration reduces the generation of curvature

compared to the catenary configuration, while the catenary configuration is more prone to generating larger curvatures in the touchdown section. The evaluation criteria for dynamic cables indicate that the catenary configuration is superior in cable tension, while the floating configuration is superior in curvature. After comprehensive consideration, Scheme Three is deemed the most suitable configuration for the dynamic cable connection between floating wind turbines and floating substations in the Hsinchu offshore area of Taiwan. This evaluation method is also considered applicable for future wind farm developers when selecting criteria for dynamic cable assessment.

As for future work, though the experimental results showed great agreement with the numerical simulations, some improvements on the experiment may be considered as follows:

1. For scaled-down mooring lines, in addition to the length, diameter, and unit weight, the spring could be attached to the end of mooring lines to offer a more precise mooring restoring force.
2. For scaled-down power cables, a more suitable material shall be found to fulfill most of the scaled-down factors, including the unit weight, axial stiffness, and bend stiffness.
3. For the image analysis of the power cable, the LEDs have been twined on rubber lines to track the motion of the power cable. The attachments would somehow influence the physical properties of the power cable, leading to some experiment errors and deviations.

Author Contributions: R.-Y.Y.: Conceptualization, Methodology, Software, Validation, Investigation, Resources, Writing—review and editing, Visualization, Supervision, Project administration, and Funding acquisition. D.-R.L.: Conceptualization, Methodology, Software, Validation, Investigation, Writing—review and editing, and Visualization. Y.-S.S.: Conceptualization, Validation, Investigation, Writing—review and editing, and Visualization. All authors have read and agreed to the published version of the manuscript.

Funding: This research was funded by the National Science and Technology Council, Taiwan, grant number NSTC 112-2221-E-006-053-MY3.

Institutional Review Board Statement: Not applicable.

Informed Consent Statement: Not applicable.

Data Availability Statement: Data is contained within the article.

Conflicts of Interest: The authors declare that they have no known competing financial interests or personal relationships that could have appeared to influence the work reported in this paper.

References

1. Yoshimoto, H.; Awashima, Y.; Kitakoji, Y.; Suzuki, H. Development of floating offshore substation and wind turbine for Fukushima FORWARD. In Proceedings of the International Symposium on Marine and Offshore Renewable Energy, Tokyo, Japan, 28–30 October 2013.
2. BW Ideol. Ideol and Atlantique Offshore Energy Launch the Commercialization of the World's First Floating Electrical Offshore Substation. 2019. Available online: <https://www.bw-ideol.com/en/ideol-and-atlantique-offshore-energy-launch-commercialization-worlds-first-floating-electrical> (accessed on 4 June 2019).
3. Shelley, S.A.; Boo, S.Y.; Kim, D.; Luyties, W.H. Concept Design of Floating Substation for a 200 MW Wind Farm for the Northeast US. In Proceedings of the Offshore Technology Conference, Houston, TX, USA, 22–25 March 2020.
4. CIGRE Working Group B1.40. *Technical Brochure 610—Offshore Generation Cable Connections*; CIRGE: Paris, France, 2015; pp. 137–141.
5. Ikhennicheu, M.; Lynch, M.; Doole, S.; Borisade, F.; Matha, D.; Dominguez, J.; Vicente, R.D.; Tim, H.; Ramitez, L.; Potestio, S.; et al. Review of the State of the Art of Mooring and Anchoring Designs, Technical Challenges and Identification of Relevant DLCs. COREWIND Project D2.1. 2020. Available online: <https://reurl.cc/VNxxmN> (accessed on 1 February 2020).
6. Thies, P.R.; Johanning, L.; Smith, G.H. Assessing mechanical loading regimes and fatigue life of marine power cables in marine energy applications. *Proc. Inst. Mech. Eng. Part O J. Risk Reliab.* **2012**, *226*, 18–32. [CrossRef]
7. Sobhania, M.; Petrini, F.; Karimirad, M.; Bontempi, F. Fatigue life assessment for power cables in floating offshore wind turbines. *Energies* **2020**, *13*, 3096. [CrossRef]

8. Srinil, N. Cabling to connect offshore wind turbines to onshore facilities. In *Offshore Wind Farms*; Woodhead Publishing: Sawston, UK, 2016; pp. 419–440. [[CrossRef](#)]
9. Shi, L.; Yang, W.; Chen, K.; Yu, G.; Jin, C.; Ni, L.; Hu, Z. Performance Evaluation of W Shape Dynamic Inter-Array Cable Configuration for Floating Offshore Wind Turbine. In Proceedings of the Offshore Technology Conference Asia, Kuala Lumpur, Malaysia, 22–25 March 2022. [[CrossRef](#)]
10. Schnepf, A.; Devulder, A.; Johnsen, Ø.; Ong, M.C.; Lopez-Pavon, C. Numerical Investigations on Suspended Power Cable Configurations for Floating Offshore Wind Turbines in Deep Water Powering an FPSO. *Offshore Mech. Arct. Eng.* **2023**, *145*, 030904. [[CrossRef](#)]
11. Beier, D.; Schnepf, A.; Van Steel, S.; Ye, N.; Ong, M.C. Fatigue Analysis of Inter-Array Power Cables between Two Floating Offshore Wind Turbines Including a Simplified Method to Estimate Stress Factors. *J. Mar. Sci. Eng.* **2023**, *11*, 1254. [[CrossRef](#)]
12. Ahmad, I.B.; Schnepf, A.; Ong, M.C. An optimization methodology for suspended inter-array power cable configurations between two floating offshore wind turbines. *Ocean. Eng.* **2023**, *278*, 114406. [[CrossRef](#)]
13. Peter, K. *Theory Manual*; ANSYS Inc.: Canonsburg, PA, USA, 2021.
14. Orcina. *OrcaFlex Manual Version 11.1b: Ulverton*; Orcina Ltd.: Cumbria, UK, 2021; Available online: <https://www.orcina.com/webhelp/OrcaFlex/Default.htm> (accessed on 19 January 2018).
15. Gaertner, E.; Rinker, J.; Sethuraman, L.; Zahle, F.; Anderson, B.; Barter, G.E.; Skrzypinski, W. *IEA Wind TCP Task 37: Definition of the IEA 15-Megawatt Offshore Reference Wind Turbine*; No. NREL/TP-5000-75698, Technical Report; U.S. Department of Energy: Denver, CL, USA, 2020.
16. Allen, C.; Viscelli, A.; Dagher, H.; Goupee, A.; Gaertner, E.; Abbas, N.; Hall, M.; Barter, G. *Definition of the UMaine VoltturnUS-S Reference Platform Developed for the IEA Wind 15-Megawatt Offshore Reference Wind Turbine*; No. NREL/TP-5000-76773, Technical Report; U.S. Department of Energy: Denver, CL, USA, 2020. [[CrossRef](#)]
17. Lai, Z.N. *Electrical and Mechanical Configuration Planning of Offshore Substation*; Taiwan Power Company: Taipei, Taiwan, 2018; Available online: <https://reurl.cc/yY8VZy> (accessed on 19 January 2018).
18. Robertson, A.; Jonkman, J.; Masciola, M.; Goupee, A.; Coulling, A.; Luan, C. *Definition of the Semisubmersible Floating System for Phase II of OC4*; No. NREL/TP-5000-60601; Technical Report; U.S. Department of Energy: Denver, CL, USA, 2014. [[CrossRef](#)]
19. *Standard DNVGL-ST-0145*; Offshore Substations. DNV GL: Høvik, Norway, 2021.
20. Janocha, M.J.; Ong, M.C.; Lee, C.F.; Chen, K.; Ye, N. Reference Power Cable Models for Floating Offshore Wind Applications. *Sustainability* **2024**, *16*, 2899. [[CrossRef](#)]
21. Rentschler, M.U.; Adam, F.; Chainho, P. Design optimization of dynamic inter-array cable systems for floating offshore wind turbines. *Renew. Sustain. Energy Rev.* **2019**, *111*, 622–635. [[CrossRef](#)]
22. *Standard DNVGL-ST-0119*; Floating Wind Turbine Structures. DNV GL: Høvik, Norway, 2018.
23. Chao, W.T.; Young, C.C. Extreme Value Analysis for Extreme Atmospheric Conditions in Taiwan Offshore Wind Farm. In Proceedings of the 42nd Ocean Engineering Conference, Keelung, Taiwan, 19–20 November 2020.
24. Chao, W.T.; Young, C.C.; Hsu, T.W. Analysis on Extreme Wind Speed Conditions under Monsoon and Typhoon Events for Offshore Wind Farm. In Proceedings of the 43rd Ocean Engineering Conference, Taoyuan, Taiwan, 18–19 November 2021.
25. *Standard DNVGL-ST-0437*; Loads and Site Conditions for Wind Turbines. DNV GL: Høvik, Norway, 2016.
26. *Offshore Standard DNVGL-RP-0286*; Recommended Practice: Coupled Analysis of Floating Wind Turbines. DNV GL: Høvik, Norway, 2019.
27. *Offshore Standard DNVGL-OS-E301*; Position Mooring. DNV GL: Høvik, Norway, 2015.
28. Karlsen, S.; Slora, R.; Heide, K.; Lund, S.; Eggertsen, F.; Osborg, P.A. Dynamic deep water power cables. In Proceedings of the 9th International Conference and Exhibition for Oil and Gas Resources Development of the Russian Arctic and CIS Continental Shelf, RAO/CIS Offshore, St Petersburg, Russian, 15–18 September 2009.
29. Miner, M. Cumulative damage in fatigue. *J. Appl. Mech.* **1945**, *12*, 159–164. [[CrossRef](#)]
30. Konispoliatis, D.N.; Mavrakos, S.A.; Chatjigeorgiou, I.K. Hydrodynamic Loading and Mooring Fatigue Estimation of an Offshore Oscillating Water Column Wave Energy Converter. In Proceedings of the 15th International Symposium on Practical Design of Ships and Other Floating Structures PRADS, Dubrovnik, Croatia, 9–13 October 2022.

Disclaimer/Publisher’s Note: The statements, opinions and data contained in all publications are solely those of the individual author(s) and contributor(s) and not of MDPI and/or the editor(s). MDPI and/or the editor(s) disclaim responsibility for any injury to people or property resulting from any ideas, methods, instructions or products referred to in the content.